Anesthesia modifies subthreshold critical slowing down in a stochastic Hodgkin-Huxley-like model with inhibitory synaptic input

Alex Bukoski,[1,*] D. A. Steyn-Ross,[2] Ashley F. Pickett,[3] and Moira L. Steyn-Ross[2]
[1]*College of Veterinary Medicine, University of Missouri, Columbia, Missouri 65211, USA*
[2]*School of Engineering, University of Waikato, Hamilton 3240, New Zealand*
[3]*College of Veterinary Medicine, Auburn University, Auburn, Alabama 36849, USA*

(Received 20 February 2018; published 7 June 2018)

The dynamics of a stochastic type-I Hodgkin-Huxley-like point neuron model exposed to inhibitory synaptic noise are investigated as a function of distance from spiking threshold and the inhibitory influence of the general anesthetic agent propofol. The model is biologically motivated and includes the effects of intrinsic ion-channel noise via a stochastic differential equation description as well as inhibitory synaptic noise modeled as multiple Poisson-distributed impulse trains with saturating response functions. The effect of propofol on these synapses is incorporated through this drug's principal influence on fast inhibitory neurotransmission mediated by γ-aminobutyric acid (GABA) type-A receptors via reduction of the synaptic response decay rate. As the neuron model approaches spiking threshold from below, we track membrane voltage fluctuation statistics of numerically simulated stochastic trajectories. We find that for a given distance from spiking threshold, increasing the magnitude of anesthetic-induced inhibition is associated with augmented signatures of critical slowing: fluctuation amplitudes and correlation times grow as spectral power is increasingly focused at 0 Hz. Furthermore, as a function of distance from threshold, anesthesia significantly modifies the power-law exponents for variance and correlation time divergences observable in stochastic trajectories. Compared to the inverse square root power-law scaling of these quantities anticipated for the saddle-node bifurcation of type-I neurons in the absence of anesthesia, increasing anesthetic-induced inhibition results in an observable exponent < -0.5 for variance and > -0.5 for correlation time divergences. However, these behaviors eventually break down as distance from threshold goes to zero with both the variance and correlation time converging to common values independent of anesthesia. Compared to the case of no synaptic input, linearization of an approximating multivariate Ornstein-Uhlenbeck model reveals these effects to be the consequence of an additional slow eigenvalue associated with synaptic activity that competes with those of the underlying point neuron in a manner that depends on distance from spiking threshold.

DOI: 10.1103/PhysRevE.97.062403

I. INTRODUCTION

Modern clinical anesthesia is a broadly successful enterprise. The ability to reversibly transition a patient between wakeful and unconscious states is both exceedingly useful and necessary for a variety of therapeutic and diagnostic purposes. However, belying the clinical use of general anesthetics is an unsatisfactory understanding of the biophysical mechanisms by which these drugs exert their profound effects. For example, consider the commonly used general anesthetic propofol whose activity is thought to be predominantly mediated through the γ-aminobutyric acid (GABA) type-A family of ligand-gated ion channels in the central nervous system (CNS) [1,2]. These channels mediate both synaptic and extrasynaptic inhibitory neural interactions [3] and propofol is known to potentiate their GABA-activated extra- to intracellular chloride currents [4]. While such molecular level effects are fairly well characterized, the mechanisms by which they propagate across the spatial and temporal scales of the mammalian CNS to produce the macroscopic state known as anesthesia are largely unknown. Studies of the electrophysiological effects of anesthetics at the micro-, meso-, and macroscopic levels of nervous tissue organization notwithstanding, this topic has garnered limited interest from the theoretical and computational communities. Among published reports, the mesoscopic mean-field approach based on modeling the average behaviors of interacting populations of excitatory and inhibitory neurons holds a prominent position [5–10], with only a handful of single neuron studies.

Using a deterministic Hodgkin-Huxley-like model including a slow potassium current (M current) and an inhibitory GABA type-A synaptic current, McCarthy and Kopell [11] demonstrated that small magnitude propofol-like effects potentiate postinhibitory rebound spiking that may contribute to observed low dose propofol-induced paradoxical excitation. Gottschalk and Haney [12] modeled halothane anesthesia in the Morris-Lecar model of the barnacle giant muscle fiber via Hill-equation-mediated reductions in the maximum conductance of the voltage-gated calcium channel. They showed the existence of two distinct regions (quiescence and sustained oscillations) in the calcium-conductance-injected current parameter space. These authors also investigated the behavior of the multicompartment Pinsky-Rinzel model of

*bukoskia@missouri.edu

CA3 hippocampal neurons. Under conditions of soma-injected current, halothane-induced reduction of maximal calcium channel conductance was shown to initially modestly increase burst frequency and duration followed by the production of high frequency sustained spike activity. Hutt and Buhry [13] showed that in the presence of excitatory synaptic activity, anesthetic-induced potentiation of extrasynaptic GABAergic inhibition influences the firing rate curves (as a function of excitatory synaptic conductance) of a type-I leaky integrate-and-fire model and a type-II Morris-Lecar model. Specifically, enhanced tonic inhibition shifts the firing rate curve to larger conductances in type-I neurons and shrinks the firing interval in type-II neurons. Consistent with the traditional theme of computational neuroscience, these studies all focus on the suprathreshold spike-forming behavior of neurons. No computational studies exist that probe the subthreshold characteristics of single neurons on approach to spiking threshold under the influence of anesthesia.

A visually distinct characteristic of single neuron membrane potential traces in the subthreshold regime on close approach to the threshold current for action potential (i.e., spike) generation is the nonlinear phenomenon known as critical slowing down (CSD). As highly nonlinear systems, the dynamical signatures of CSD—growth in amplitude simultaneous with decay in frequency of fluctuations about a stable fixed point—have been observed in transmembrane potential traces from both experimental and computational work on single neurons. The first published report of CSD in this setting was by Matsumoto and Kunisawa [14] in 1978 using the squid giant axon preparation (a type-II resonator system that undergoes an Andronov-Hopf birfurcation and upon which the classical Hodgkin-Huxley model is based). More recently, CSD was experimentally observed in pyramidal neurons (a type-I integrator system that undergoes a saddle-node bifurcation) in rat acute neocortical slices as a function of distance from spiking threshold [15]. Critical slowing has also been shown to develop in simulated voltage trajectories of type-I and type-II model neurons as a natural consequence of intrinsic biological noise modeled as either additive white-noise [16] or via Markov chain descriptions of stochastic voltage-gated ion channel dynamics [17]. Notably, using mean-field theory it has been proposed that the observable surge in electroencephalographic power at anesthetic-induced loss of consciousness—known as the biphasic effect [18,19]—results from critically slowed fluctuations of an average excitatory "soma voltage" state variable that grow in magnitude as anesthesia modulates an inhibitory neurotransmitter rate constant thereby driving the system toward a transition point between two stable branches of a fixed point manifold [20,21]. Within this "anesthetodynamic" phase transition framework, CSD is induced by the combination of noisy subcortical drive and the external constraint of propofol-like anesthesia; neither alone is sufficient.

Given these findings, we seek to characterize the influence of anesthesia on the subthreshold dynamics of single neurons using stochastic Hodgkin-Huxley-like models. This topic, to the best of our knowledge, has not been previously investigated and the current investigation represents a theoretical contribution whose experimental verification remains an open question. Specifically, we investigate the influence of propofol-like GABAergic anesthesia on CSD in a type-I mammalian pyramidal point neuron model endowed with stochastic ion channel kinetics and driven by random inhibitory GABA type-A synaptic activity on close approach to spiking threshold. For biologically motivated parameters we demonstrate that anesthetic-induced augmentation of inhibitory synaptic interactions modifies the intrinsic critically slowed dynamics of the transmembrane potential trajectory. Notably, anesthesia tends to enhance the qualitative signatures of critical slowing down—voltage fluctuation amplitude, correlation time, and spectral power at 0 Hz are all increased—over a range of dimensionless distances from spiking threshold. On closer approach to threshold, this trend breaks down with both the variances and correlation times converging to common values. However, while the qualitative features of CSD are retained, anesthesia significantly modifies the anticipated inverse square root power-law scalings for saddle-node bifurcation. For variance and correlation time, divergences observable in simulated stochastic trajectories display exponents less than and greater than -0.5, respectively. Using a linearized Ornstein-Uhlenbeck approximation of the full model, we show that this behavior is due to anesthetic-induced alterations in the model's underlying eigenvalue structure. An additional slow eigenvalue associated with synaptic activity, that is significantly influenced by anesthesia, competes with those of the underlying point neuron for dominance. Linear theory predicts that synaptic dynamics will dominate unless distance from threshold is sufficiently diminished at which point the dynamics of the underlying bifurcation structure of the type-I neuron emerge. Independently of anesthesia, collapse of the signatures of CSD in stochastic trajectories on close approach to threshold noted above is the result of increasingly nonlinear behavior necessary for spike generation.

II. MODEL

We consider a synaptically driven Hodgkin-Huxley-like point neuron model. In its most general form the model is

$$C\frac{dV}{dt} = I_{\mathrm{DC}} - g_{\mathrm{Na}}(t)(V - E_{\mathrm{Na}}) - g_{\mathrm{K}}(t)(V - E_{\mathrm{K}}) - g_{\mathrm{L}}(V - E_{\mathrm{L}}) - I_{\mathrm{syn}}, \tag{1}$$

where V is transmembrane potential measured with respect to the extracellular environment; C is membrane capacitance; I_{DC} is an injected stimulus current; $g_{\mathrm{Na}}(t)$ and $g_{\mathrm{K}}(t)$ are time-dependent total sodium and potassium channel conductances; g_{L} is the leakage channel conductance; and E_{Na}, E_{K}, and E_{L} are, respectively, the sodium, potassium, and leakage ion channel reversal potentials. The last term, I_{syn}, is the total current induced by synaptic interactions where here we consider only inhibitory synapses designed to model phasic GABA type-A input. Note that if I_{syn} is set to zero and the sodium and potassium channel dynamics are described deterministically such that $g_{\mathrm{Na}}(t) \to \bar{g}_{\mathrm{Na}} m^3 h$ and $g_{\mathrm{K}}(t) \to \bar{g}_{\mathrm{K}} n^4$, the traditional form of the Hodgkin-Huxley model [22],

$$C\frac{dV}{dt} = I_{\mathrm{DC}} - \bar{g}_{\mathrm{Na}} m^3 h(V - E_{\mathrm{Na}}) - \bar{g}_{\mathrm{K}} n^4 (V - E_{\mathrm{K}}) - g_{\mathrm{L}}(V - E_{\mathrm{L}}), \tag{2a}$$

$$\frac{dx}{dt} = \alpha_x(V)(1 - x) - \beta_x(V)x, \tag{2b}$$

TABLE I. Voltage-dependent gating variable rate constants for the Nowotny and Rabinovich [29,30] parametrization of the Eq. (2) deterministic type-I integrator model as well as the Figs. 1 and 2 Markov chains. Rate constant units are ms^{-1} and voltage, V, is measured in mV.

Symbol	Function
$\alpha_n(V)$	$-0.032(V+50)/\{\exp[-(V+50)/5]-1\}$
$\alpha_m(V)$	$-0.32(V+52)/\{\exp[-(V+52)/4]-1\}$
$\alpha_h(V)$	$0.128\exp[-(V+48)/18]$
$\beta_n(V)$	$0.5\exp[-(V+55)/40]$
$\beta_m(V)$	$0.28(V+25)/\{\exp[(V+25)/5]-1\}$
$\beta_h(V)$	$4/\{\exp[-(V+25)/5]+1\}$

is recovered. Here $\bar{g}_{\mathrm{Na}}$ and $\bar{g}_{\mathrm{K}}$ are the maximum sodium and potassium channel conductances; $x \in \{n,m,h\}$ where n, m, and h are gating variables that describe the kinetics of potassium channel activation, sodium channel activation, and sodium channel inactivation, respectively; and the $\alpha_x(V)$ and $\beta_x(V)$ functions are transmembrane potential-dependent first-order rate constants for gate opening and closing (see Table I). Although biologically motivated, this deterministic model fails to account for the significant influence of thermally induced random state transitions responsible for the observed stochastic dynamics of ion channels. In order to incorporate these effects with those of synaptic noise on transmembrane potential dynamics, we use stochastic descriptions of both the ion channel kinetics, $g_{\mathrm{Na}}(t)$ and $g_{\mathrm{K}}(t)$, and synaptic interactions, I_{syn}.

A. Channel-based stochastic differential equation

The mathematical description of ion channel stochasticity is typically achieved via one of two general approaches: continuous time, discrete state Markov chains or their diffusion approximations. Considered the default gold standard method, Markov chains are accurate but extremely time consuming to numerically simulate—even when implemented using efficient methods such as the Gillespie algorithm [23]. For the sodium and potassium channels of the Eq. (2) Hodgkin-Huxley-like model, the corresponding Markov chains that provide the correct deterministic (i.e., large channel number) limiting behavior are given in Figs. 1 and 2. Formulated by Fox and Lu [24] as a method to approximate the fraction of channels

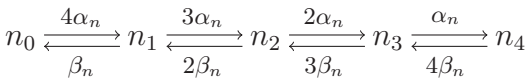

FIG. 1. Markov-chain model (kinetic scheme) of the Hodgkin-Huxley potassium channel with four activation n gates. There are five states in total, each characterized by a different number of open gates, and eight possible state transitions. The only fully open and conducting state is n_4. State subscripts indicate the number of open n gates and voltage-dependent transition rates are given next to the associated arrow. The potassium channel state occupancy vector is $\mathbf{X}_{\mathrm{K}} = [X_0, X_1, X_2, X_3, X_4]^{\mathrm{T}}$ with $X_{\mathrm{K}}^{\mathrm{open}} = X_4$. See Table I for definitions of the α_n and β_n rates.

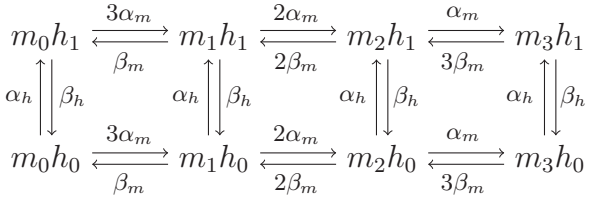

FIG. 2. Markov-chain model (kinetic scheme) of the Hodgkin-Huxley sodium channel with three activation m gates and one inactivation h gate. There are a total of eight states, each characterized by a different number of open gates, and twenty possible state transitions. The only fully open and conducting state is m_3h_1. State subscripts indicate the number of open m and h gates and transition rates are given next to the associated arrow. The sodium channel state occupancy vector is $\mathbf{Y}_{\mathrm{Na}} = [Y_{00}, Y_{10}, Y_{20}, Y_{30}, Y_{01}, Y_{11}, Y_{21}, Y_{31}]^{\mathrm{T}}$ with $Y_{\mathrm{Na}}^{\mathrm{open}} = Y_{31}$. See Table I for definitions of the α_m, α_h, β_m, and β_h rates.

in each Markov state in a large ensemble of Markov chains, the diffusion approximation utilizes multivariate stochastic differential equations (SDEs) with appropriately weighted white-noise perturbations. In this approach, the sodium and potassium conductances are described as $g_i = \bar{g}_i\, f_i^{\mathrm{open}}$ for $i \in \{\mathrm{Na},\mathrm{K}\}$, where f_i^{open} is the fraction of open channels and $\bar{g}_i$ is the maximal conductance. Of the available diffusion approximations, we follow [25] and write the so-called channel-based model as

$$C\frac{dV}{dt} = I_{\mathrm{DC}} - \bar{g}_{\mathrm{Na}} Y_{\mathrm{Na}}^{\mathrm{open}}(V - E_{\mathrm{Na}}) - \bar{g}_{\mathrm{K}} X_{\mathrm{K}}^{\mathrm{open}}(V - E_{\mathrm{K}}) - g_{\mathrm{L}}(V - E_{\mathrm{L}}), \tag{3a}$$

$$\frac{d\mathbf{Y}_{\mathrm{Na}}}{dt} = \mathbf{A}_{\mathrm{Na}}\mathbf{Y}_{\mathrm{Na}} + \frac{1}{\sqrt{N_{\mathrm{Na}}}}\mathbf{S}_{\mathrm{Na}}(\mathbf{Y}_{\mathrm{Na}})\boldsymbol{\xi}_{\mathrm{Na}}(t), \tag{3b}$$

$$\frac{d\mathbf{X}_{\mathrm{K}}}{dt} = \mathbf{A}_{\mathrm{K}}\mathbf{X}_{\mathrm{K}} + \frac{1}{\sqrt{N_{\mathrm{K}}}}\mathbf{S}_{\mathrm{K}}(\mathbf{X}_{\mathrm{K}})\boldsymbol{\xi}_{\mathrm{K}}(t), \tag{3c}$$

where $\mathbf{Y}_{\mathrm{Na}}$ and $\mathbf{X}_{\mathrm{K}}$ are 8- and 5-element column vectors containing each channel's state occupancy fractions (see Figs. 1 and 2); $\mathbf{A}_{\mathrm{Na(K)}}$ is the sodium (potassium) channel drift matrix; $\mathbf{S}_{\mathrm{Na(K)}} = \sqrt{\mathbf{D}_{\mathrm{Na(K)}}}$ with $\mathbf{D}_{\mathrm{Na(K)}}$ the state-occupancy-dependent sodium (potassium) channel diffusion matrix; $N_{\mathrm{Na(K)}}$ is the total number of sodium (potassium) channels being modeled; and $\boldsymbol{\xi}_{\mathrm{Na}}(t)$ and $\boldsymbol{\xi}_{\mathrm{K}}(t)$ are multivariate independent Gaussian white-noise processes delta-correlated in time (i.e., infinite variance) with zero mean. Exact expressions for the $\mathbf{A}_{\mathrm{Na(K)}}$ and $\mathbf{S}_{\mathrm{Na(K)}}$ matrices can be found in Ref. [25]. Note that this model is consistent with the deterministic behavior of Eq. (2) in the limit of large membrane area, A, via the relationships $N_{\mathrm{Na(K)}} = A\,\rho_{\mathrm{Na(K)}}$, where $\rho_{\mathrm{Na(K)}}$ are the channel densities.

While generally computationally more efficient than direct simulation of the associated Markov chains, the class of diffusion approximations are not without numerical difficulties. Reviewed in [26], these include maintaining physically meaningful boundary conditions and normalization (i.e., $X_i \in [0,1]$ and $\sum X_i = 1$ for some state vector $\mathbf{X}$) on the fractional state occupancies of each channel. If these constraints are violated it becomes possible for the square root of the diffusion matrix to produce unphysical complex values. In response,

various formulations of the diffusion approximation have been proposed, each characterized by the methods employed to circumvent these issues. As demonstrated in [26] and [27], the implementation due to Orio and Soudry [25] is the most satisfactory based on numerical comparisons. These authors used a novel method to directly write the **S** matrices from the Markov chain diagrams, thereby avoiding the matrix square root operation necessary when the diffusion matrix is used to numerically obtain **S**. Although this formulation does not directly address the boundary constraint, the normalization requirement can be implemented within the numerical algorithm thereby modeling a reduced 12-variable system rather than the original 14-variable system. In addition, and most importantly, this approach has been shown to give results statistically indistinguishable from Markov chain simulations for channel numbers in excess of approximately 10^3. For smaller channel numbers, direct Markov chain simulation may be the most appropriate and efficient choice [27]. Because the model parametrizations used here correspond to sodium and potassium channel numbers of order $\sim 10^4$, we utilize the Orio and Soudry [25] diffusion approximation to directly incorporate ion channel noise.

B. Synaptic interactions

The total synaptic current, $I_{\rm syn}$ in Eq. (1), due to phasic GABA type-A inhibitory input is given by

$$I_{\rm syn} = g_{\rm GABA}(t)(V - E_{\rm GABA}), \tag{4}$$

where $g_{\rm GABA}(t)$ is the total inhibitory synaptic conductance per unit area and $E_{\rm GABA}$ is the inhibitory synaptic reversal potential. To model $g_{\rm GABA}(t)$, we imagine $N_{\rm syn}$ inhibitory synapses incident on a neural membrane of area A such that this total conductance can be expressed as

$$\begin{aligned} g_{\rm GABA}(t) &= \bar{g}_{\rm GABA}\left(\frac{1}{N_{\rm syn}}\sum_{i=1}^{N_{\rm syn}} r_i(t)\right) \\ &= \bar{g}_{\rm GABA} R(t), \end{aligned} \tag{5}$$

where $r_i(t)$ is the inhibitory synaptic response function of the ith synapse, $\bar{g}_{\rm GABA}$ is the maximum specific conductance due to all inhibitory synaptic interactions, and the quantity $R(t)$ represents the proportion of this maximal conductance realized at time t. The time dependence of each $r_i(t)$ is described by the ordinary differential equation [28]

$$\frac{dr_i}{dt} = \alpha\, T_i(t)(1 - r_i) - \frac{\beta}{\gamma}\, r_i, \tag{6}$$

driven by a train of presynaptic rectangular impulses, $T_i(t)$, Poisson distributed in time with mean rate λ. Here α and β/γ describe the kinetics of the rise and fall of the synaptic response, respectively, and $\gamma \geqslant 1$ is a dimensionless parameter used to simulate the effect of increasing concentration of the GABAergic anesthetic agent propofol on the decay rate, with $\gamma = 1$ corresponding to no anesthesia. When $\gamma > 1$, decay of the synaptic response is prolonged resulting in enhanced synaptic inhibition. This modeling approach is consistent with experimental observations [4] and captures the essential feature of anesthetics which, generally speaking, induce loss of consciousness in a concentration dependent manner. In this sense, the γ parameter captures the notion of "anesthetic effect," a term used frequently throughout this paper. Note that $T_i(t)$ is a shot noise process with a rectangular response function and that both $r_i(t)$ and $R(t)$ are saturating processes contained in the interval $[0,1]\forall t$. The synaptic response to a single (i.e., unitary) presynaptic impulse is shown in Fig. 3 as a function of the anesthetic effect parameter γ. To make closer contact with the channel-based SDE model and its dependence on the area of membrane being modeled, note that $\bar{g}_{\rm GABA}$ can also be expressed as $g^{\rm syn}_{\rm GABA} N_{\rm syn}/A$ where $g^{\rm syn}_{\rm GABA}$ is the maximum individual synaptic conductance.

C. Full stochastic model

Combining Eqs. (1) and (3)–(6), the full model investigated in this study is given by the following set of equations:

$$\begin{aligned} C\frac{dV}{dt} &= I_{\rm DC} - \bar{g}_{\rm Na} Y^{\rm open}_{\rm Na}(V - E_{\rm Na}) \\ &\quad - \bar{g}_{\rm K} X^{\rm open}_{\rm K}(V - E_{\rm K}) - g_{\rm L}(V_m - E_{\rm L}) \\ &\quad - \bar{g}_{\rm GABA} R\,(V - E_{\rm GABA}), \end{aligned} \tag{7a}$$

$$\frac{d\mathbf{Y}_{\rm Na}}{dt} = \mathbf{A}_{\rm Na}\mathbf{Y}_{\rm Na} + \frac{1}{\sqrt{N_{\rm Na}}}\mathbf{S}_{\rm Na}(\mathbf{Y}_{\rm Na})\boldsymbol{\xi}_{\rm Na}(t), \tag{7b}$$

$$\frac{d\mathbf{X}_{\rm K}}{dt} = \mathbf{A}_{\rm K}\mathbf{X}_{\rm K} + \frac{1}{\sqrt{N_{\rm K}}}\mathbf{S}_{\rm K}(\mathbf{X}_{\rm K})\boldsymbol{\xi}_{\rm K}(t), \tag{7c}$$

$$\frac{dr_i}{dt} = \alpha\, T_i(t)(1 - r_i) - \frac{\beta}{\gamma}\, r_i, \tag{7d}$$

where $i \in \{1,2,\ldots,N_{\rm syn}\}$. To complete these equations, we parametrize them in two steps. First, for the channel-based SDE portion, we use the parameter set from Nowotny and Rabinovich [29,30], based on the mammalian hippocampal pyramidal cell model of Traub and Miles, that describes type-I integrator behavior (see Table II). Based on previous work [17], the membrane area is set to 3000 μm^2 in order to sufficiently attenuate ion channel noise-induced spontaneous subthreshold spike production. Treating $I_{\rm DC}$ as the bifurcation parameter, in the absence of inhibitory synaptic input this model undergoes a deterministic saddle-node bifurcation at $I_{\rm DC} \approx 0.35577$ μA cm^{-2}. Note that the parameters given in [29] and [30] have been scaled here to a standard specific capacitance value of 1 μF cm^{-2}. For the second step, we parametrize the GABA type-A synaptic response function according to the work of Destexhe *et al.* [28] whereby $\alpha = 5$ ms^{-1} mM^{-1}, $\beta = 0.18$ ms^{-1}, and each presynaptic rectangular GABA impulse has width 1 ms and magnitude 1 mM (see Fig. 3). The inhibitory synaptic reversal potential, $E_{\rm GABA}$, is set to -70 mV [31].

The remaining free parameters, $\bar{g}_{\rm GABA}$, $N_{\rm syn}$, and λ, are more challenging to constrain. In part, this is due to nontrivial difficulties associated with taking physiologic data obtained from real neurons with spatial extent and nonuniform distributions of synaptic contacts and distilling these to values appropriate for a model devoid of spatial scale. To address this issue, we again look to the work of Destexhe and co-workers [32] who developed a pyramidal neuron "point conductance" model from both electrophysiological whole cell recordings and morphologically reconstructed multicompartment biophysical

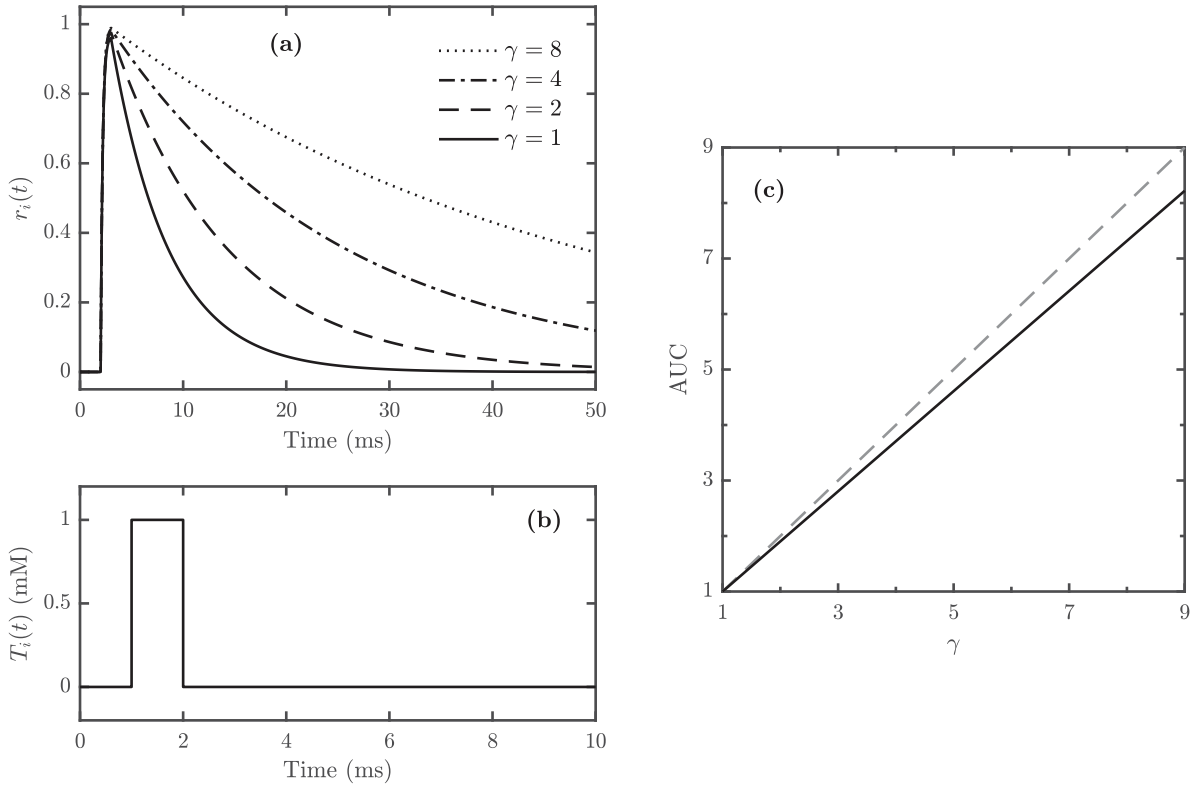

FIG. 3. Anesthesia is modeled (a) by reducing the unitary synaptic response $r_i(t)$ (i.e., the response to a single presynaptic impulse) decay rate, β, of Eq. (6) via the parameter $\gamma \geqslant 1$. The condition of no anesthesia corresponds to $\gamma = 1$ and the effective decay rate of the response is β/γ while the characteristic timescale of the decay is γ/β. Presynaptic activity is modeled (b) using 1 ms wide rectangular impulses of magnitude 1 mM [28]. (c) The integrated area under the unitary synaptic response curve (AUC), normalized to the $\gamma = 1$ value, as a function of γ. This quantity is anticipated to be proportional to the total charge transferred during a unitary response. Modeling propofol's influence on the synaptic response decay rate using the γ parameter, including the resultant linear relationship between AUC and γ, is consistent with experimental observations [4].

models that included physiologic data on synaptic distributions and conductances. For excitatory and inhibitory synaptic conductances, these authors found Ornstein-Uhlenbeck SDEs to satisfactorily model their overall impact in the reduced "point conductance" model. Across four different neuronal morphologies, the mean and standard deviation of the total inhibitory specific conductances were reported [32] to be of order ∼0.1 and ∼0.01 mS cm^{-2}. Guided by this work, we initially explored values of $\bar{g}_{\mathrm{GABA}}$, N_{syn}, and λ consistent with these results as well as with synaptic densities and firing rates reported in the literature. Because such parameter sets admitted excessively high near-threshold spike-forming behavior in simulated stochastic trajectories, we ultimately focused on $\bar{g}_{\mathrm{GABA}} = 0.1$ mS cm^{-2}, $N_{\mathrm{syn}} = 300$, and $\lambda = 5$ Hz. In the absence of anesthesia (i.e., for $\gamma = 1$), these parameters give an inhibitory synaptic conductance with mean and standard deviation ∼0.003 and ∼0.0007 mS cm^{-2}. These lower values compared to those of Ref. [32] were used to attenuate near threshold spike formation and allow for sufficiently long epochs of spike-free activity for analysis. However, we note broad agreement of the qualitative findings reported here over a range of parameters including $30 \leqslant N_{\mathrm{syn}} \leqslant 1500$ and $5 \leqslant \lambda \leqslant 20$ Hz. For all parameter sets, subthreshold transmembrane potential dynamics were explored as a function of both dimensionless proximity to threshold, $\epsilon = (I_{\mathrm{DC}}^{\mathrm{crit}} - I_{\mathrm{DC}})/I_{\mathrm{DC}}^{\mathrm{crit}}$, and anesthetic effect parameter, $\gamma \in \{1,2,4,8\}$.

TABLE II. Model constants for the mammalian pyramidal neuron model due to Nowotny and Rabinovich [29,30] which demonstrates type-I integrator behavior.

Symbol	Value	Unit
C	1	μF cm^{-2}
E_{Na}	50	mV
E_{K}	−95	mV
E_{L}	−63.563	mV
$\bar{g}_{\mathrm{Na}}$	50	mS cm^{-2}
$\bar{g}_{\mathrm{K}}$	10	mS cm^{-2}
g_{L}	0.187	mS cm^{-2}
ρ_{Na}	60	channels μm^{-2}
ρ_{K}	18	channels μm^{-2}
$I_{\mathrm{DC}}^{\mathrm{crit}}$	≈ 0.35577	μA cm^{-2}

D. Critical current for spike formation

Because we focus on subthreshold transmembrane potential behavior as a function of proximity to spiking threshold,

ϵ, and magnitude of anesthetic effect, γ, it is necessary to determine, for each parameter set, the critical input current for spike formation, $I_{\rm DC}^{\rm crit}$. The value of $I_{\rm DC}^{\rm crit}$ is defined within a deterministic framework wherein the sodium and potassium channel conductances are described by their traditional Hodgkin-Huxley forms [see Eq. (2)] and synaptic contributions are taken in the mean. For the parametrization used here, the model's saddle-node bifurcation at $I_{\rm DC}^{\rm crit}$ is located as the $I_{\rm DC}$ value at which the number of fixed points transitions from three to one. Fixed points of the model are determined by setting all time derivatives to zero and substituting for the m_∞, n_∞, and h_∞ steady-state values of the gating variables as well as for the mean total synaptic activation, μ_R [see Eq. (9)], to obtain

$$0 = I_{\rm DC} - \bar{g}_{\rm Na} m_\infty^3 h_\infty (V - E_{\rm Na}) - \bar{g}_{\rm K} n_\infty^4 (V - E_{\rm K}) - g_{\rm L}(V - E_{\rm L}) - \bar{g}_{\rm GABA}\mu_R (V - E_{\rm GABA}). \quad (8)$$

The $I_{\rm DC}^{\rm crit}$ value is then numerically located using a bisection search algorithm on the number of transmembrane potential fixed points.

One difficulty in this process is due to the saturating nature of differential equation (7d) describing the synaptic response variables [i.e., both $r_i(t)$ and $R(t)$ are confined to the unit interval]. Despite being driven by Poisson-distributed impulses, it is not possible to analytically solve for the mean and variance of $R(t)$ (as is possible for nonsaturating response functions using Campbell's theorem). Rather, we obtain estimates of these quantities by numerically simulating long realizations of the $R(t)$ process via

$$\mu_R = \frac{1}{T}\int_0^T R(t)dt \approx \frac{\Delta t}{T}\sum_j R(t_j), \quad (9)$$

$$\sigma_R^2 = \frac{1}{T}\int_0^T [R(t) - \mu_R]^2 dt \approx \frac{\Delta t}{T}\sum_j [R(t_j) - \mu_R]^2, \quad (10)$$

where T is the total simulation time and, typically, $T \sim 10^5$ ms. Note that the necessity to numerically estimate the value of μ_R results in slight variation of the realized value from one simulation to the next due to pseudorandom production of the Poisson-distributed driving impulses. Uncertainty in the value of μ_R translates to uncertainty in the computed values of $I_{\rm DC}^{\rm crit}$ and, therefore, in the values of the applied current for set proximity parameter ϵ via $I_{\rm DC} = (1-\epsilon)I_{\rm DC}^{\rm crit}$. This introduces a problem: as $\epsilon \to 0$ (i.e., as $I_{\rm DC} \to I_{\rm DC}^{\rm crit}$), there is an ever increasing risk of unknowingly exceeding the true $I_{\rm DC}^{\rm crit}$ value and thereby simulating suprathreshold, rather than subthreshold, voltage trajectories. Numerical studies of the propagation of uncertainty in μ_R to $I_{\rm DC}^{\rm crit}$ suggest that at $\epsilon = 0.01$, the likelihood of accidentally exceeding $I_{\rm DC}^{\rm crit}$ is minimal (see Table III). In practice, suprathreshold trajectories are quite difficult to reliably distinguish from their close-to-threshold subthreshold counterparts due to the nature of type-I neuron dynamics wherein the emergence of spike formation occurs at arbitrarily low rates. Consequently, for $\epsilon \lesssim 0.01$, contamination of stochastic voltage trajectory realizations with unintended suprathreshold trajectories is possible. However, given that noise is an innate feature of biology to which neurons are constantly exposed, complete discrimination between the sub- and suprathreshold regimes may not be desirable or meaningful.

TABLE III. Dependence of uncertainty in the numerical determination of the mean total synaptic activation, μ_R, on the anesthetic effect parameter, γ, and propagation of that error to determinations of the total synaptic activation variance, σ_R^2, and critical current for spike formation, $I_{\rm DC}^{\rm crit}$. These illustrative data are for $\bar{g}_{\rm GABA} = 0.1$ mS cm^{-2}, $\lambda = 5$ Hz, and $N_{\rm syn} = 300$ and are based on 100 independent 10^5 ms long realizations of the $R(t)$ process. Data are presented as mean $\pm$ one standard deviation.

γ	μ_R	$\sigma_R^2(\times 10^{-4})$	$I_{\rm DC}^{\rm crit}$ (μA cm^{-2})
1	0.02974 ± 0.00007	0.5025 ± 0.0055	0.3862 ± 0.0001
2	0.05517 ± 0.00013	0.8716 ± 0.0134	0.4122 ± 0.0001
4	0.1022 ± 0.0002	1.479 ± 0.031	0.4604 ± 0.0002
8	0.1832 ± 0.0004	2.308 ± 0.067	0.5445 ± 0.0004

E. Linearization

Following [16] and [17], we linearize the full model to gain insight into the numerical simulation results. Because a straightforward linearization is not possible due to the presence of the Poisson-distributed driving term in Eq. (6), we approximate the overall effect of the inhibitory synapses by replacing the $N_{\rm syn}$ differential equations for the $r_i(t)$ variables with a single Ornstein-Uhlenbeck (OU) process designed to mimic their influence. Specifically, we linearize the modified Eq. (7) system

$$C\frac{dV}{dt} = I_{\rm DC} - \bar{g}_{\rm Na} Y_{\rm Na}^{\rm open}(V - E_{\rm Na}) - \bar{g}_{\rm K} X_{\rm K}^{\rm open}(V - E_{\rm K}) - g_{\rm L}(V_m - E_{\rm L}) - \bar{g}_{\rm GABA}\tilde{R}\,(V - E_{\rm GABA}), \quad (11a)$$

$$\frac{d\mathbf{Y}_{\rm Na}}{dt} = \mathbf{A}_{\rm Na}\mathbf{Y}_{\rm Na} + \frac{1}{\sqrt{N_{\rm Na}}}\mathbf{S}_{\rm Na}(\mathbf{Y}_{\rm Na})\boldsymbol{\xi}_{\rm Na}(t), \quad (11b)$$

$$\frac{d\mathbf{X}_{\rm K}}{dt} = \mathbf{A}_{\rm K}\mathbf{X}_{\rm K} + \frac{1}{\sqrt{N_{\rm K}}}\mathbf{S}_{\rm K}(\mathbf{X}_{\rm K})\boldsymbol{\xi}_{\rm K}(t), \quad (11c)$$

$$\frac{d\tilde{R}}{dt} = -\frac{1}{\tau}(\tilde{R} - \mu_R) + \sqrt{D}\,\xi_{\tilde{\rm R}}(t), \quad (11d)$$

where $\tau = \gamma/\beta$, μ_R is given by Eq. (9), $D = 2\sigma_R^2/\tau$, and the $\tilde{R}(t)$ process approximates the $R(t)$ process. The relationships defining the τ and D parameters of the approximating OU process in Eq. (11) have been adopted from [33] and are strictly only exact for an OU process approximating a large number of independent shot-noise processes with nonsaturating exponential response functions.

By explicitly implementing the normalization requirements to eliminate the X_0 and Y_{00} variables, we work with a reduced 13-variable system and linearize about the steady-state $\mathbf{Z}^0 = [V^0, X_1^0, X_2^0, X_3^0, X_4^0, Y_{10}^0, Y_{20}^0, Y_{30}^0, Y_{01}^0, Y_{11}^0, Y_{21}^0, Y_{31}^0, \tilde{R}]^{\rm T}$ to form the multivariate OU process

$$\frac{d}{dt}\mathbf{z}(t) = -\mathbf{A}\mathbf{z}(t) + \mathbf{S}\Xi(t), \quad (12)$$

where $\mathbf{z}(t) = \mathbf{Z}(t) - \mathbf{Z}^0$ is a 13-element column vector containing the fluctuation of each variable about its steady-state value; $\mathbf{A}$ is the 13×13 drift matrix of the aggregate system; $\mathbf{S}$ is the 13×16 square root of the diffusion matrix of the aggregate system; and Ξ is a column vector containing the independent

white-noise perturbations with $\Xi_1 = 0$ (i.e., there is no direct noise perturbation of the transmembrane potential). Note that the **S** matrix has block diagonal form $\mathbf{S} = \mathrm{diag}(0, \mathbf{S}_K, \mathbf{S}_{Na}, \sqrt{D})$ with the dimensions of $\mathbf{S}_K$ and $\mathbf{S}_{Na}$ being, respectively, 4×4 and 7×10. The drift matrix, **A**, is equal to the negative of the Jacobian matrix, **J**, of Eqs. (11) evaluated at the nominated steady state (i.e., $\mathbf{A} = -\mathbf{J}$)

$$\mathbf{J} = \left. \frac{\partial(F_V, F_{X_1}, \ldots, F_{Y_{31}}, F_{\tilde{R}})}{\partial(V, X_1, \ldots, Y_{31}, \tilde{R})} \right|_{\mathbf{Z}^0}. \tag{13}$$

Note that there is no simple relationship between the drift matrix **A** of Eq. (12) and the $\mathbf{A}_{K(Na)}$ matrices of Eqs. (11b) and (11c), unlike the direct relationship between **S** and $\mathbf{S}_{K(Na)}$. See the Appendix for additional details on the linearization.

Stationary solutions to Eq. (12) will exist in the subthreshold regime where each of the 13 eigenvalues, $0 > \lambda_1 \geqslant \lambda_2 \geqslant \cdots \geqslant \lambda_{13}$, of the Jacobian matrix are negative or have negative real part. Note that the inverse of the real part of each eigenvalue defines a characteristic timescale for the dynamical development of perturbations in a region close to the steady state. The dominant (i.e., the least negative) eigenvalue, λ_1, determines the slowest of these timescales: $T_{\mathrm{slow}} = -1/\lambda_1$.

Following Gardiner [34], stochastic calculus gives the general solution to Eq. (12) in the subthreshold regime as

$$\mathbf{A}\Sigma + \Sigma\mathbf{A}^{\mathrm{T}} = \mathbf{S}\mathbf{S}^{\mathrm{T}}, \tag{14}$$

where Σ is the 13×13 covariance matrix. The Σ_{11} element of the covariance matrix gives the variance, $\mathrm{var}\{\delta v\}$, of transmembrane potential deviations, $\delta v(t) = V(t) - V^0$, about the V^0 steady state at each input current. To capture the essential components of dynamical slowing—growth in amplitude simultaneous with decay in frequency of transmembrane potential fluctuations—we consider the probability density of fluctuations together with the time-correlation matrix and its Fourier transform, the spectrum matrix. For the Eq. (11) multivariate, linear OU process, the probability density of voltage fluctuations is predicted to be Gaussian with zero mean and variance given by Σ_{11}. The time-correlation matrix, $\mathbf{C}(\tau)$, with symmetry property $\mathbf{C}(-\tau) = [\mathbf{C}(\tau)]^{\mathrm{T}}$, is given by [34]

$$\mathbf{C}(\tau) = e^{-\mathbf{A}\tau}\Sigma, \tag{15}$$

where $\tau \geqslant 0$ is the time lag. Likewise, the spectrum matrix, $\mathbf{G}(\omega)$, is given by [34]

$$\mathbf{G}(\omega) = \frac{1}{2\pi}(\mathbf{A} + i\omega\mathbf{I})^{-1}\mathbf{S}\mathbf{S}^{\mathrm{T}}(\mathbf{A}^{\mathrm{T}} - i\omega\mathbf{I})^{-1}, \tag{16}$$

where ω is frequency, i is the imaginary unit, and **I** is the identity matrix. Note that the linear analysis presented here is only applicable in the subthreshold regime: on crossing threshold at least one eigenvalue of the Jacobian matrix will satisfy $\mathrm{Re}(\lambda_i) > 0$ and a stationary solution to Eq. (12) will no longer exist.

Predictions derived from Eqs. (14), (15), and (16) are compared to transmembrane potential fluctuation statistics obtained from numerical simulation of the full stochastic model. When combined with eigenvalue analysis of the Jacobian matrix, the linearized system is used to provide insight into the observed dynamical behavior on approach to threshold.

III. NUMERICAL SIMULATIONS

The full stochastic model, Eq. (7), was implemented in MATLAB, version 2016b. All computations were preformed using double-precision (64-bit) floating-point arithmetic. We simulated stochastic transmembrane potential trajectories as a function of dimensionless proximity to threshold (ϵ) for various combinations of the mean rate of inhibitory impulses (λ), the number of synaptic connections (N_{syn}), the anesthetic effect parameter (γ), and the maximal conductance of the inhibitory synaptic interactions ($\bar{g}_{\mathrm{GABA}}$). Spike detection in simulated traces was accomplished via an algorithm based on the transmembrane potential crossing a threshold value (typically chosen to be 0 mV). For each detected spike, both the prior and subsequent 50 ms of simulated time were excluded from analysis. Increasing these exclusion times did not significantly influence the fluctuation statistics computed from the spike-free epochs likely due to minimal overall spike formation (<5 Hz) in the majority, but not all, of the simulated trajectories (the likelihood of spike formation increases as $\epsilon \to 0$). Simulation times of 20.5 s were used for each parameter set at each ϵ value. The initial conditions for each simulation corresponded to the average input current density dependent deterministic equilibrium state. The first 0.5 s of each simulated trace was discarded prior to analysis. The Euler-Maruyama algorithm was used for numerical integration with a deterministic time step $\Delta t = 0.005$ ms. Over the range of conditions considered here, the smallest timescale associated with either the underlying point neuron model or the synaptic dynamics was ~0.09 ms—an order of magnitude larger than this time step—and simulations using $\Delta t = 0.001$ ms did not influence the results. For each γ value, transmembrane potential trajectories were simulated for $1 \leqslant \epsilon \leqslant 0.001$ with $\epsilon \to 0$ corresponding to increasingly close approach to spiking threshold. To account for uncertainty in $I_{\mathrm{DC}}^{\mathrm{crit}}$ values for each $\{\lambda, \bar{g}_{\mathrm{GABA}}, \gamma, N_{\mathrm{syn}}\}$ parameter set—as illustrated in Table III—100 independent transmembrane potential trajectories were computed for each parameter combination at each ϵ value.

To characterize the subthreshold behavior of the model for each parameter set, we computed probability distribution densities, autocorrelation functions, and power spectral densities of subthreshold voltage fluctuations, δv. Probability densities were estimated from their respective voltage time series by computing transmembrane potential fluctuation histograms and then dividing by $N\Delta V$ with $N = 2001$ the number of bins and ΔV the bin width. Autocorrelation functions were computed with the MATLAB *xcorr* function by averaging autocorrelations from 2000 ms non-overlapping segments. Power spectral densities were computed with the MATLAB *spectrogram* function using a top-hat window and 100 ms epochs with 50% overlap. Linearized predictions were obtained from Eqs. (15) and (16) by first solving Eq. (14) for the covariance matrix, Σ, using the MATLAB *sylvester* function.

IV. RESULTS

Sample transmembrane potential stochastic trajectories are presented in Fig. 4 to illustrate the impact of anesthesia on the subthreshold dynamics of the Eq. (7) full stochastic model. There are noticeable increases in the magnitude and

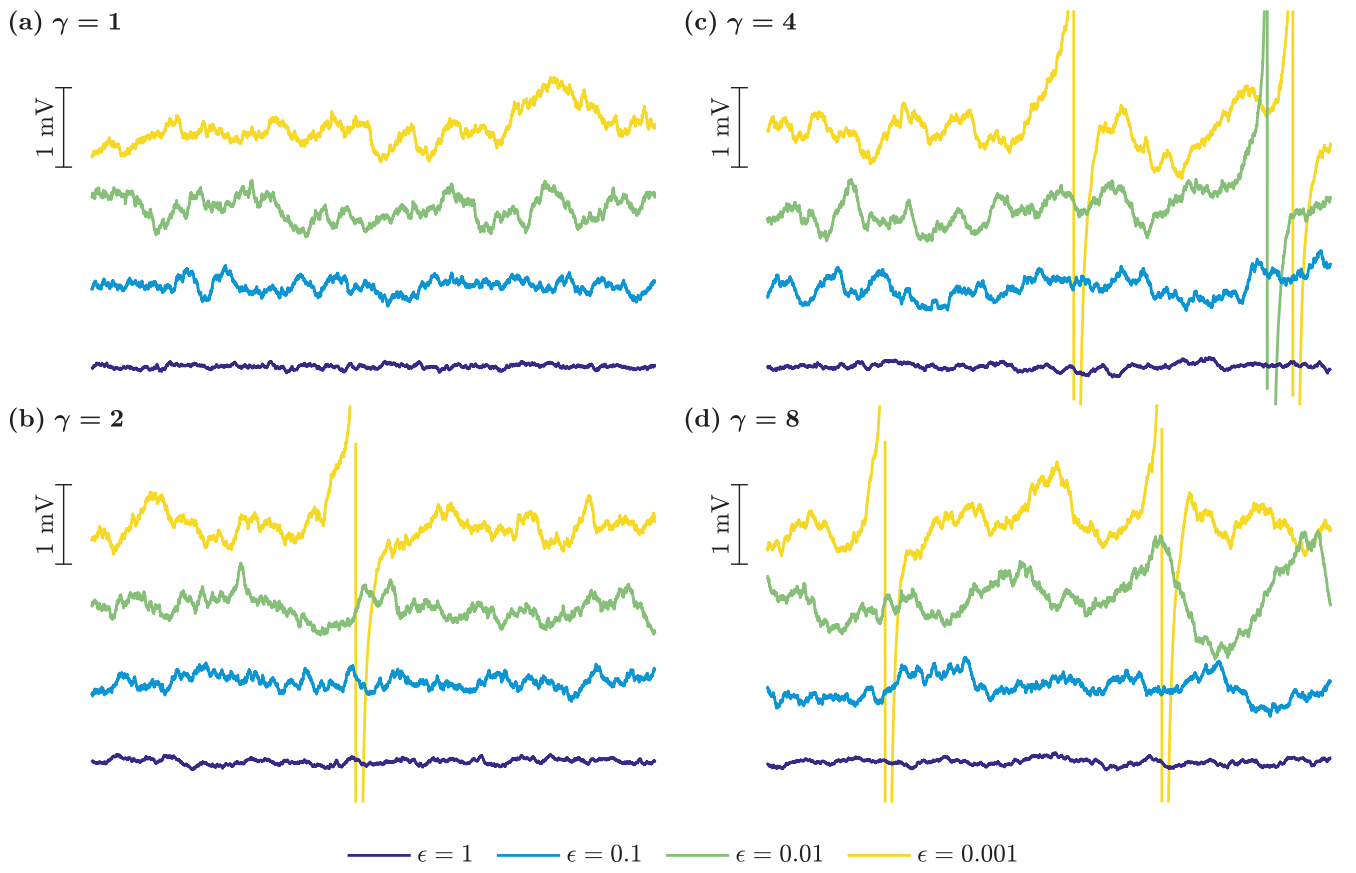

FIG. 4. Raw 1 s duration transmembrane potential stochastic trajectories computed from the Eq. (7) full model for order-of-magnitude reductions of the dimensionless distance from spiking threshold, $\epsilon = (I_{DC}^{crit} - I_{DC})/I_{DC}^{crit}$ (see legend), and various levels of anesthetic effect [(a) $\gamma = 1$, (b) $\gamma = 2$, (c) $\gamma = 4$, and (d) $\gamma = 8$]. For those trajectories that include spikes, discontinuities are an artifact of suppressing full spike magnitudes. These illustrative traces are for $\bar{g}_{GABA} = 0.1$ mS cm^{-2}, $\lambda = 5$ Hz, and $N_{syn} = 300$. Trajectories have been offset vertically for consistent alignment and to reduce overlap.

duration of subthreshold excursions from equilibrium as the distance from spiking threshold, ϵ, approaches zero and as the anesthetic effect parameter, γ, increases. To quantify these effects, voltage fluctuation statistics computed from multiple realizations of the full stochastic model are given in Fig. 5 for the same sequence of order-of-magnitude differences in proximity to spiking threshold and γ values. Column 1 gives probability density functions (PDFs) which are seen to grow in breadth—corresponding to growth in voltage fluctuation amplitude—as $\epsilon \to 0$ for set γ and as γ increases for set ϵ. However, for $\epsilon \lesssim 0.01$ it appears that PDF width becomes increasingly less dependent on γ concurrent with the appearance of negative skew indicating departure from the symmetric, Gaussian predictions of linear theory. The predominance of negative fluctuations is consistent with the lack of excitatory synaptic input in the full model such that lower membrane potentials are favored in the subthreshold regime. Overall, these observations for $\epsilon \lesssim 0.01$, despite deletion of all spiking activity prior to analysis, are consistent with the increasingly significant role of nonlinear dynamics as $\epsilon \to 0$ (i.e., as $I_{DC} \to I_{DC}^{crit}$): spike formation at threshold is an inherently nonlinear phenomenon. Note that for $\epsilon = 0.01$ and 0.001, the PDF thorns appearing at $\delta v = 0$ are an artifact of spike exclusion from the raw voltage trajectories and serve as a visual indicator of stochastic spike formation. Columns 2 and 3 of Fig. 5 give power spectral densities (PSDs) and autocorrelation functions (ACFs) for the same ϵ and γ values as for column 1. Qualitatively consistent with the dynamics of critical slowing down, we observe growth in the 0 Hz component of the PSDs and in the width of the ACFs for increasing γ and decreasing ϵ. However, as for PDF width discussed above, these trends break down for $\epsilon \lesssim 0.01$ indicating the appearance of nonlinear behavior necessary for spike emergence at threshold.

The trends in stochastic trajectory fluctuation variance and correlation time noted in Fig. 5, together with their eventual collapse as $\epsilon \to 0$, are readily apparent in Figs. 6 and 7(a), respectively. In addition, these figures clearly illustrate the presence of divergences in these quantities as $\epsilon \to 0$ for set γ as well as a γ-dependent enhancement of variance and correlation time for set ϵ. The collapse of these behaviors for $\epsilon \lesssim 0.01$, with both the variances and correlation times trending toward common values regardless of anesthetic effect, is also easier to quantify. In addition to fluctuation statistics computed from stochastic trajectories, Figs. 6 and 7(a) provide mean variance and correlation time predictions computed from linearization of the approximating multivariate OU process. Agreement between linear theory and full stochastic model statistics is shown to be excellent for $\epsilon > 0.01$ but breaks down for $\epsilon < 0.01$.

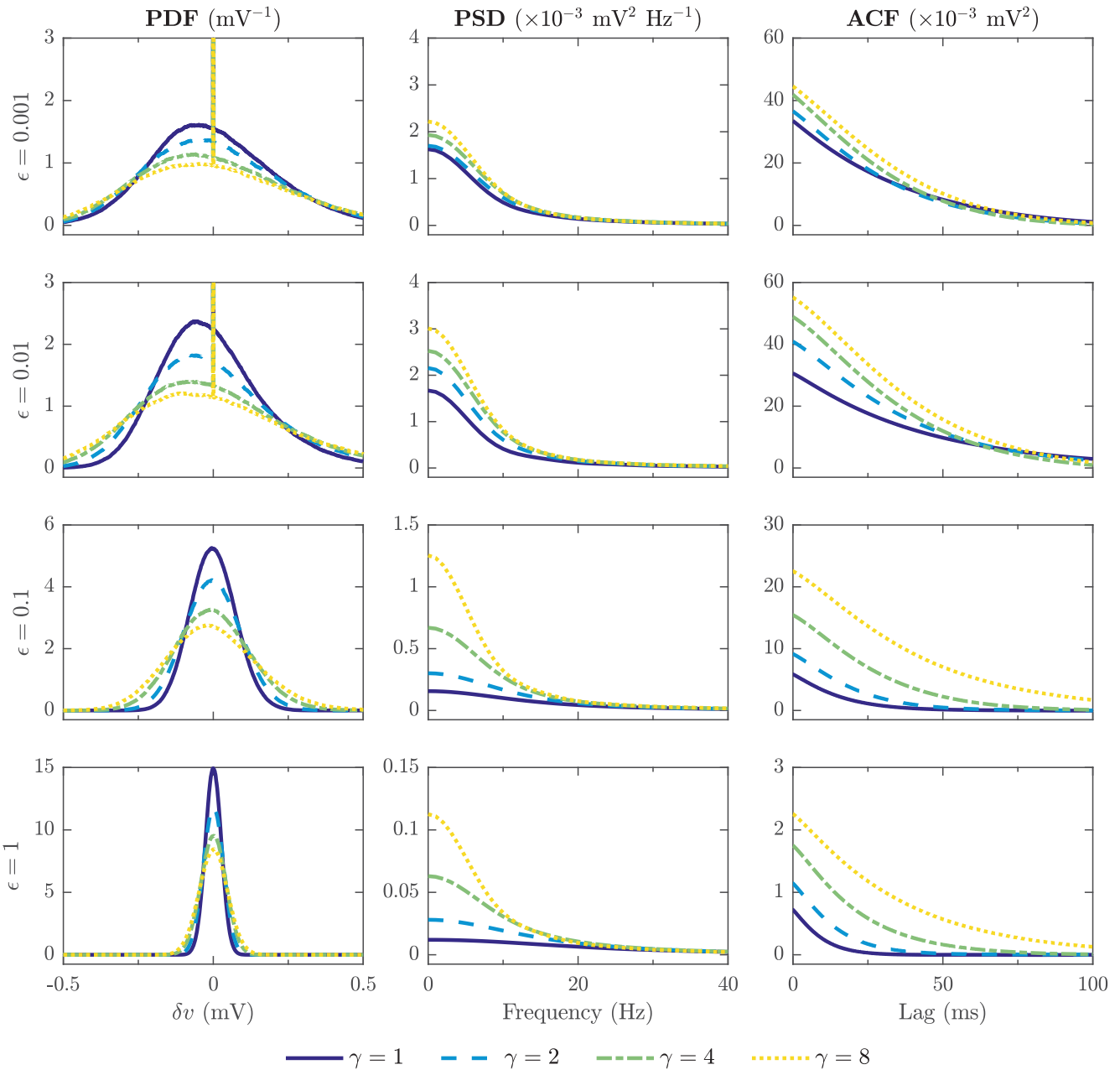

FIG. 5. Transmembrane potential fluctuation probability density functions (PDF; column 1), power spectral densities (PSD; column 2), and autocorrelation functions (ACF; column 3) for variable proximity to spiking threshold, ϵ (decreases from row 4 to row 1), and anesthetic effect parameter, γ (see legend), for $\bar{g}_{\mathrm{GABA}} = 0.1$ mS cm^{-2}, $\lambda = 5$ Hz, and $N_{\mathrm{syn}} = 300$. Each curve is an average of the results for 100 independent realizations of the underlying transmembrane potential trajectories. Appropriate units for the ordinates of each column are given in the column heading. The thorns riding on top of the $\epsilon = 0.01$ and 0.001 PDFs are a signature artifact generated by spike exclusion from raw voltage trajectories.

For the linear theory predictions in both Figs. 6 and 7(a), there is eventual convergence to $1/\sqrt{\epsilon}$ scaling behavior as $\epsilon \to 0$ for all γ values as expected for the saddle-node bifurcation of type-I neuron dynamics. Notably, this behavior is never fully realized in the statistics computed from stochastic trajectories due to the appearance of nonlinearities necessary for spike formation. A final observation from these figures is that power-law divergence exponents for mean fluctuation statistics from simulated stochastic trajectories based on results for $\epsilon \gtrsim 0.01$ would give values < -0.5 for variance divergence and > -0.5 for correlation time divergence when $\gamma > 1$. Thus the quantitative $1/\sqrt{\epsilon}$ divergence scalings characteristic of the saddle-node bifurcation of the underlying point neuron are not observable but the qualitative trends associated with critical slowing are preserved as a function of both proximity to threshold and anesthetic effect. In this way, anesthesia modifies critical slowing down by altering the quantitative aspects, while retaining the qualitative aspects, of this nonlinear phenomenon.

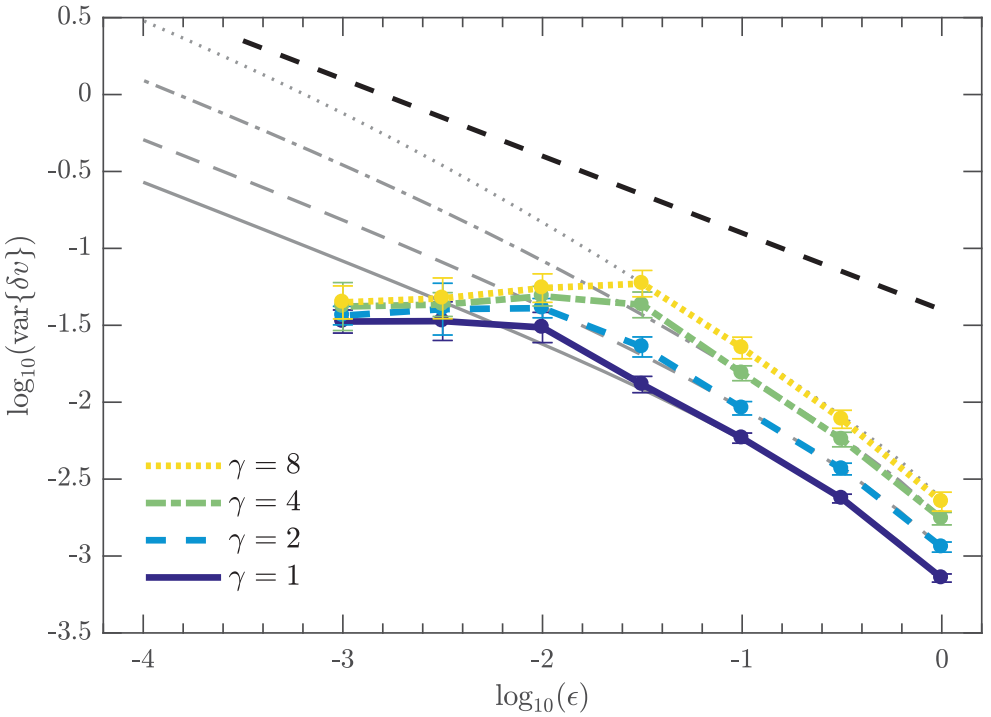

FIG. 6. Divergence of transmembrane potential fluctuation variance in the Eq. (7) type-I integrator neuron model with inhibitory synaptic input as a function of proximity to instability threshold, ϵ, and anesthetic effect parameter, γ, for $\bar{g}_{\mathrm{GABA}} = 0.1$ mS cm^{-2}, $\lambda = 5$ Hz, and $N_{\mathrm{syn}} = 300$. Thick color (gray scale) lines represent results computed from simulation of the Eq. (7) full stochastic model and thinner gray dashed lines represent predictions based on linearization of the Eq. (11) Ornstein-Uhlenbeck system. Results are based on 100 independent transmembrane potential trajectories computed for each $\{\epsilon,\gamma\}$ pair. For the full model, error bars represent $\pm$ two standard deviations while only mean results are presented for the linear model. The topmost thick dashed black line has a slope of -0.5 for reference. Note that for all γ values the linear OU divergences approach $1/\sqrt{\epsilon}$ as $\epsilon \to 0$ but this behavior is never fully realized in the stochastic trajectories which converge towards a common value starting at $\epsilon \sim 0.01$.

Also shown in Fig. 7(b) are the timescales corresponding to the two most dominant eigenvalues of the approximating linearized OU model. For each value of the anesthetic effect parameter γ, there is an associated threshold proximity, ϵ, where the dominant eigenvalue transitions from a constant value to divergence with ϵ as $1/\sqrt{\epsilon}$. Prior to these transitions, the dominant timescales for $\gamma = 1, 2, 4$, and 8 are, respectively, 6.1, 11.1, 22.2, 44.4 ms. These values closely track the characteristic timescales of the inhibitory synaptic decay, given by γ/β, which are 5.6, 11.1, 22.2, and 44.4 ms for the same gamma values. The exception to this behavior is the $\gamma = 1$ case wherein the dominant timescale is divergent over the entire ϵ range investigated. These results indicate that, within the linear approximation, the behavior of the full model as $\epsilon \to 0$ can be explained by a dynamical competition between the underlying point neuron and synapses: there is an initial dominance of synaptic activity followed by emergence of the point neuron dynamics. This emergence is possible because of the constant nature of the synaptic dynamics which are independent of proximity to threshold. Additionally, the extent to which the characteristic subthreshold divergences of the underlying point neuron are observed in stochastic trajectories is determined by an interplay between the appearance of nonlinearity necessary for spike formation, leading to the eventual collapse of divergences, and the influence of synaptic interactions as affected by anesthesia. To illustrate this effect, consider the results shown in Fig. 7. For $\gamma = 1$, the ϵ value in Fig. 7(b) at which eigenvalue dominance shifts from synaptic to point neuron dynamics is effectively unity and, comparing the stochastic trajectory results of Fig. 7(a), this curve most rapidly conforms to the anticipated -0.5 divergence exponent as ϵ decreases. At the other extreme, the $\gamma = 8$ curve in Fig. 7(a) never fully attains a divergence exponent of -0.5 because divergence collapse due to nonlinearity occurs at approximately the same ϵ value [i.e., at $\log_{10}(\epsilon) \sim -2$] at which the eigenvalue dominance changes. In this case, the dynamics of the underlying point neuron model are effectively masked by the synaptic dynamics.

Note that results have been presented in Figs. 5, 6, and 7 using the dimensionless parameter $\epsilon = (I_{\mathrm{DC}}^{\mathrm{crit}} - I_{\mathrm{DC}})/I_{\mathrm{DC}}^{\mathrm{crit}}$ because nonlinear dynamics predicts that the signatures of critical slowing down should scale with distance from threshold (i.e., proximity to bifurcation) and not the magnitude of the bifurcation parameter. Given that $I_{\mathrm{DC}}^{\mathrm{crit}}$ varies with γ (see Table III) and that ion channel dynamics are voltage dependent, this raises the question of the comparability of mean subthreshold voltages between trajectories characterized by different γ values for some particular ϵ value. Mean voltages computed from spike-deleted stochastic realizations for set ϵ values but different γ values reveals agreement to within 0.5 mV. This indicates

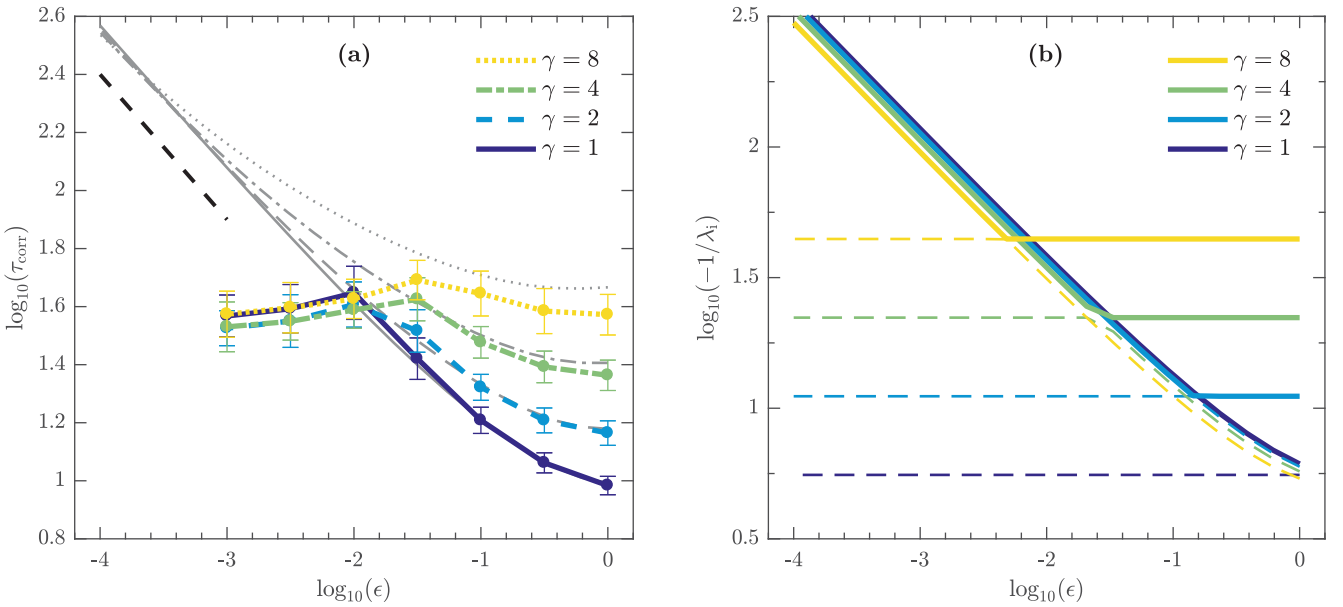

FIG. 7. (a) Divergence of correlation times, $\tau_{\rm corr}$, for transmembrane potential fluctuations computed as the time required for the autocorrelation function to decay to $1/e$ of the zero-lag peak. Thick color (gray scale) lines represent results computed from simulation of the Eq. (7) full stochastic model and thinner gray dashed lines represent predictions based on linearization of the Eq. (11) Ornstein-Uhlenbeck (OU) system. For the full model, error bars represent $\pm$ two standard deviations while only mean results are presented for the linear model. The thick dashed black line has a slope of -0.5 for reference. Note that for all γ values the linear OU divergences approach $1/\sqrt{\epsilon}$ as $\epsilon \to 0$. However, this behavior is never fully realized in the stochastic trajectories which converge toward a common value of $\sim$40 ms for $\epsilon \lesssim 0.01$. (b) Mean behavior of the two largest characteristic times $\tau_i = -1/\lambda_i$ with $i = 1,2$ predicted from the two largest eigenvalues, λ_i with $0 > \lambda_1 \geqslant \lambda_2$, of the linearized Eq. (11) OU system. For each γ value, τ_1 is given by the solid line and τ_2 by the dashed line. In both (a) and (b), results are presented as a function of proximity to instability threshold, ϵ, and anesthetic effect parameter, γ, for $\bar{g}_{\rm GABA} = 0.1\,{\rm mS\,cm^{-2}}$, $\lambda = 5\,{\rm Hz}$, and $N_{\rm syn} = 300$. All results are based on 100 independent transmembrane potential trajectories computed for each $\{\epsilon, \gamma\}$ pair.

that the effects of γ presented here are not due to underlying variation of ion channel dynamics induced by dissimilar mean voltages.

V. DISCUSSION

Extending our previous work [17] on the subthreshold dynamics of stochastic Hodgkin-Huxley-like point neuron models to include inhibitory synaptic interactions and the effect of GABAergic anesthetics such as propofol, we have demonstrated how anesthesia modifies the observable statistical signatures of critical slowing down as a model point neuron approaches spiking threshold from below. Specifically, qualitative features including growth of fluctuation amplitude, focusing of spectral power toward 0 Hz, and increasing correlation time as spiking threshold is approached from below, for a set magnitude of anesthetic-induced inhibition, are retained. Additionally, these same features are enhanced by augmented anesthetic-induced inhibition for set proximity to threshold (see Figs. 6 and 7). Prior to collapse of these trends due to the necessary emergence of highly nonlinear spike-forming dynamics on sufficiently close approach to threshold, the quantitative inverse square root divergences for fluctuation variance and correlation time of the underlying point neuron model's saddle-node bifurcation structure as threshold is approached from below are increasingly difficult to observe in stochastic trajectories as the effect of anesthesia is increased due to an anesthetic-enhanced dominance of synaptic dynamics. Linearization of an approximating multivariate Ornstein-Uhlenbeck process was used to illustrate the dynamical mechanism underpinning this behavior: the addition of an eigenvalue associated with the synaptic dynamics to those of the bare point neuron model. Because this eigenvalue is independent of distance from spiking threshold, there exists a competition for dominance between it and those of the underlying point neuron which continuously diverge as the system moves closer to spike formation. Within the linear approximation the system must make a sufficiently close approach to spiking threshold for the saddle-node bifurcation dynamics to fully emerge. Importantly, anesthesia tends to suppress this emergence by augmenting the dominance of the eigenvalue associated with the synaptic dynamics. Despite excellent agreement between linear theory and the full stochastic model for moderate distances from spiking threshold, divergence between these linear predictions and the statistics of stochastic trajectories is significant at about 1% from threshold presumably due to the increasing importance of nonlinear behavior (i.e., the dynamics of spike formation that must necessarily emerge at threshold).

Our principal motivations for studying the influence of anesthesia on neuronal dynamics in the subthreshold regime were twofold. First, because suprathreshold spike-forming behavior (i.e., neurocomputational properties traditionally defined by the statistics of spike formation such as interspike intervel distributions) must necessarily emerge from the subthreshold regime, alterations of subthreshold dynamics may be a significant contributor to alterations in suprathreshold

dynamics. For example, although it is well known that different bifurcation structures—such as the saddle-node bifurcation of type-I neurons and the Andronov-Hopf bifurcation of type-II neurons—lead to characteristic firing rate behaviors, the introduction of random perturbations to such systems has been demonstrated to have complex dynamical effects. In their study of the Morris-Lecar model parametrized to achieve either type-I or type-II behavior, Tateno and Pakdaman [35] found that while additive white noise destroys the bifurcation structures that characterize these classes of activity (in the sense of the evolution of probability densities), the reliability of stimulus-evoked responses in each class was maintained. Other interesting effects of additive noise on the spike-forming characteristics of neural models have also been reported including the inhibition, rather than enhancement, of spiking by weak noise (see [36], [37], and references therein).

Our second motivation for carrying out this work is broad interest in the mechanisms by which anesthetics exert their wide ranging effects on the central nervous system including effects at the single neuron level. As suggested in the Introduction, how anesthetics influence the dynamics of single neurons and how these effects translate across the spatiotemporal domains of the central nervous system are open questions. As externally and dynamically applied constraints on inherently nonlinear neural structures which function far from equilibrium, anesthetics clearly give rise to a massively useful and interesting phenomenon. In relation to the work presented here, to the extent that anesthetics at clinically relevant concentrations reduce spike formation in single neurons, these findings imply that the synaptic influence of GABAergic anesthesia on single neuron dynamics in the subthreshold regime is more complex than a straightforward enhancement of inhibition. To this point, our model predicts that GABAergic anesthesia will enhance, rather than diminish, the variance of subthreshold voltage fluctuations.

The significance of these findings for the mechanisms by which anesthetics induce and maintain unconsciousness is unclear. To our knowledge, critical slowing down has not been observed at the single neuron level during anesthetic-induced loss of consciousness. This contrasts with the prediction of mean-field cortical models that the biphasic effect observed in electroencephalographic recordings during loss of consciousness *is* an observable manifestation of critical slowing down of an excitatory mesoscopic state variable. Because a necessary and sufficient condition for loss of consciousness has not been defined—other than the administration of anesthetics—it would be premature to speculate on the position of the current work in the context of anesthesia as an integrated whole.

However, in the single neuron setting we believe that the effects of GABAergic anesthesia illustrated by our model could be tested in an electrophysiological laboratory using suitable neural preparations via, perhaps, the dynamic clamp methodology of Destexhe and co-workers [33] designed to mimic the collective behavior of realistic synaptic interactions. However, based on the recent work of Meisel and colleagues [15] who provided the first quantitative evidence of critical slowing using whole-cell patch-clamp recordings from pyramidal neurons and fast-spiking interneurons in rat acute neocortical slices, this may be critically dependent on the magnitude of synaptic noise. As they note in [15] regarding the use of observable signatures of critical slowing to predict the occurrence of bifurcations, "Although prediction performance is naturally impeded by stochastic perturbations which can trigger critical transitions even before the bifurcation point is reached ... given sufficient data and moderate noise levels, reasonable quantitative predictions become possible." The results given here suggest that the ability to detect such signatures will critically depend not only on the noise magnitude but also on the dynamical interaction between the characteristics of the synaptic noise and those of the neuron being exposed to the noise. Despite this reservation, a scenario in which these findings could have biological significance is for subthreshold neuron-to-neuron communication via electrical gap junctions. Although the exact role of electrical gap junctions is currently unclear, they have been hypothesized to play a significant dynamical role in the cerebrum in mean-field theories by supporting the formation of large-scale Turing structures [38]. If the subthreshold signatures of critical slowing are utilized as a means of interneuron communication, the results presented here suggest that anesthesia has the potential to significantly modify this mechanism.

Regarding limitations of the current work, there are several considerations. These include (i) the use of a constant input current, I_{DC}, to drive the model toward threshold in a controlled manner in favor of more realistic excitatory synaptic interactions that would be present *in vivo*, (ii) the use of uniform inhibitory synapses when in fact there is known to be a great diversity of GABA receptor subtypes [39], and (iii) the inclusion of only the principal effect of propofol which is also known to influence the dynamics of voltage-gated ion channels [40] as well as the rates of presynaptic impulses [41,42]. Such synaptic and ion channel effects could be significant on close approach to threshold given the dynamics of competition between synapses and point neuron demonstrated here. Additionally, appropriately parametrizing a spatially reduced model is a nontrivial task for the reasons noted in Sec. II C. In this respect, the $\bar{g}_{\mathrm{GABA}}$ parameter may be the most significant as it primarily controls the overall magnitude of the inhibitory synaptic input. We note that numerical simulations carried out for $\bar{g}_{\mathrm{GABA}} = 0.01$ mS cm^{-2}, a value 10-fold lower than that used here, give results consistent with what would be expected in the $\bar{g}_{\mathrm{GABA}} \to 0$ limit: regression to the behavior demonstrated for the stochastic point neuron model without synaptic input [17]. On the other hand, increasing $\bar{g}_{\mathrm{GABA}}$ by an order of magnitude to 1 mS cm^{-2} results in complete dominance of the synaptic interactions. For GABA type-A maximal specific conductances intermediate to these extremes, the qualitative results described here are consistently observed.

As noted by an anonymous referee, despite their popularity in computational neuroscience studies, single-compartment Hodgkin-Huxley-like models—while biologically motivated—lack the phenomenologically realistic rapid spike initiation dynamics observed in cortical neurons [43,44]. Despite using spike-deleted stochastic trajectories for computation of the statistical signatures of critical slowing down, this dynamical deficiency could potentially impact the results presented here. This is because we studied dynamics as a function of the threshold proximity parameter, ϵ, as $\epsilon \to 0$. Aside from using computationally more intensive multicompartment models endowed with suitable ion channel dynamics [43],

models with defined thresholds such as those in the integrate-and-fire (IF) family [45] could be utilized to investigate the influence of spike initiation dynamics on the results reported here. While defined threshold models would circumvent the problems associated with defining the critical currents for spike formation noted in Sec. II D, it is unclear how to include realistic ion channel noise. Likewise, it would be important to select a model, such as the quadratic IF model, that incorporates a suitable bifurcation structure (e.g., the leaky IF model is linear and thus incapable of demonstrating critical slowing down). These issues are deserving of further study given that spike initiation dynamics may have functional consequences in neural ensembles communicating via suprathreshold spike trains [46].

One aspect of this work that is perhaps surprising is the overall robustness of linear theory in the subthreshold regime in the presence of synaptic input. In addition to excellent general agreement with statistics obtained from stochastic trajectories, linearization provides a dynamical explanation for the observed results: the inverse square root scaling characteristic of saddle-node bifurcations is effectively masked by the timescales of the synaptic interactions such that the variance scaling exponent can appear less than -0.5 and the correlation time scaling exponent can appear greater than -0.5. This implies that observable scalings from stochastic trajectories are predicted to approach the anticipated -0.5 exponent for situations in which the dynamical impact of the synaptic interactions is reduced such as for reduced presynaptic firing rates which, importantly, may result from the effects of anesthetics [41,42].

In conclusion, we have shown that the effects of GABAergic anesthesia on inhibitory synapses modifies the characteristics of subthreshold critical slowing in a type-I Hodgkin-Huxley-like model that includes stochastic ion channel dynamics. While it is well known that ion channel stochasticity can lead to the generation of spontaneous action potentials, there are few studies that explicitly include these dynamics when other noise sources are present. Based on previous work [17], we used a stochastic differential equation description to capture this component of neural dynamics and added inhibitory synaptic noise modeled to allow straightforward inclusion of the effects of GABAergic anesthetics like propofol. We find that while anesthesia both enhances and retains the qualitative features of critical slowing on approach to spiking threshold, it also significantly modifies the anticipated inverse square root scaling behavior for divergence of the voltage fluctuation variance and correlation time. To the best of our knowledge, this is the first computational study of the subthreshold effects of anesthetics and the predictions presented here have not been reported in experimental preparations. Future experimental work is required to determine the presence and significance of these results in neural tissue.

APPENDIX: LINEARIZATION

The Eq. (11) approximating multivariate Ornstein-Uhlenbeck channel-based model is composed of the following system of 15 stochastic differential equations:

$$
\begin{aligned}
C\frac{dV}{dt} &= I_{\mathrm{DC}} - \bar{g}_{\mathrm{Na}}Y_{31}(V-E_{\mathrm{Na}}) - \bar{g}_{\mathrm{K}}X_4(V-E_{\mathrm{K}}) - g_{\mathrm{L}}(V-E_{\mathrm{L}}) - \bar{g}_{\mathrm{GABA}}\tilde{R}(V-E_{\mathrm{GABA}}),\\
\frac{dX_0}{dt} &= -4\alpha_n X_0 + \beta_n X_1 + \sqrt{4\alpha_n X_0 + \beta_n X_1}\frac{\xi_1^{\mathrm{K}}(t)}{\sqrt{N_{\mathrm{K}}}},\\
\frac{dX_1}{dt} &= 4\alpha_n X_0 - \beta_n X_1 - 3\alpha_n X_1 + 2\beta_n X_2 - \sqrt{4\alpha_n X_0 + \beta_n X_1}\frac{\xi_1^{\mathrm{K}}(t)}{\sqrt{N_{\mathrm{K}}}} + \sqrt{3\alpha_n X_1 + 2\beta_n X_2}\frac{\xi_2^{\mathrm{K}}(t)}{\sqrt{N_{\mathrm{K}}}},\\
\frac{dX_2}{dt} &= 3\alpha_n X_1 - 2\beta_n X_2 - 2\alpha_n X_2 + 3\beta_n X_3 - \sqrt{3\alpha_n X_1 + 2\beta_n X_2}\frac{\xi_2^{\mathrm{K}}(t)}{\sqrt{N_{\mathrm{K}}}} + \sqrt{2\alpha_n X_2 + 3\beta_n X_3}\frac{\xi_3^{\mathrm{K}}(t)}{\sqrt{N_{\mathrm{K}}}},\\
\frac{dX_3}{dt} &= 2\alpha_n X_2 - 3\beta_n X_3 - \alpha_n X_3 + 4\beta_n X_4 - \sqrt{2\alpha_n X_2 + 3\beta_n X_3}\frac{\xi_3^{\mathrm{K}}(t)}{\sqrt{N_{\mathrm{K}}}} + \sqrt{\alpha_n X_3 + 4\beta_n X_4}\frac{\xi_4^{\mathrm{K}}(t)}{\sqrt{N_{\mathrm{K}}}},\\
\frac{dX_4}{dt} &= \alpha_n X_3 - 4\beta_n X_4 - \sqrt{\alpha_n X_3 + 4\beta_n X_4}\frac{\xi_4^{\mathrm{K}}(t)}{\sqrt{N_{\mathrm{K}}}},\\
\frac{dY_{00}}{dt} &= -3\alpha_m Y_{00} + \beta_m Y_{10} - \alpha_h Y_{00} + \beta_h Y_{01} + \sqrt{3\alpha_m Y_{00} + \beta_m Y_{10}}\frac{\xi_1^{\mathrm{Na}}(t)}{\sqrt{N_{\mathrm{Na}}}} + \sqrt{\alpha_h Y_{00} + \beta_h Y_{01}}\frac{\xi_4^{\mathrm{Na}}(t)}{\sqrt{N_{\mathrm{Na}}}},\\
\frac{dY_{10}}{dt} &= 3\alpha_m Y_{00} - \beta_m Y_{10} - 2\alpha_m Y_{10} + 2\beta_m Y_{20} - \alpha_h Y_{10} + \beta_h Y_{11} - \sqrt{3\alpha_m Y_{00} + \beta_m Y_{10}}\frac{\xi_1^{\mathrm{Na}}(t)}{\sqrt{N_{\mathrm{Na}}}}\\
&\quad + \sqrt{2\alpha_m Y_{10} + 2\beta_m Y_{20}}\frac{\xi_2^{\mathrm{Na}}(t)}{\sqrt{N_{\mathrm{Na}}}} + \sqrt{\alpha_h Y_{10} + \beta_h Y_{11}}\frac{\xi_5^{\mathrm{Na}}(t)}{\sqrt{N_{\mathrm{Na}}}},\\
\frac{dY_{20}}{dt} &= 2\alpha_m Y_{10} - 2\beta_m Y_{20} - \alpha_m Y_{20} + 3\beta_m Y_{30} - \alpha_h Y_{20} + \beta_h Y_{21} - \sqrt{2\alpha_m Y_{10} + 2\beta_m Y_{20}}\frac{\xi_2^{\mathrm{Na}}(t)}{\sqrt{N_{\mathrm{Na}}}}\\
&\quad + \sqrt{\alpha_m Y_{20} + 3\beta_m Y_{30}}\frac{\xi_3^{\mathrm{Na}}(t)}{\sqrt{N_{\mathrm{Na}}}} + \sqrt{\alpha_h Y_{20} + \beta_h Y_{21}}\frac{\xi_6^{\mathrm{Na}}(t)}{\sqrt{N_{\mathrm{Na}}}},
\end{aligned}
$$

$$
\begin{aligned}
\frac{dY_{30}}{dt} &= \alpha_m Y_{20} - 3\beta_m Y_{30} - \alpha_h Y_{30} + \beta_h Y_{31} - \sqrt{\alpha_m Y_{20} + 3\beta_m Y_{30}}\frac{\xi_3^{\mathrm{Na}}(t)}{\sqrt{N_{\mathrm{Na}}}} + \sqrt{\alpha_h Y_{30} + \beta_h Y_{31}}\frac{\xi_7^{\mathrm{Na}}(t)}{\sqrt{N_{\mathrm{Na}}}},\\
\frac{dY_{01}}{dt} &= -3\alpha_m Y_{01} + \beta_m Y_{11} + \alpha_h Y_{00} - \beta_h Y_{01} + \sqrt{3\alpha_m Y_{01} + \beta_m Y_{11}}\frac{\xi_8^{\mathrm{Na}}(t)}{\sqrt{N_{\mathrm{Na}}}} - \sqrt{\alpha_h Y_{00} + \beta_h Y_{01}}\frac{\xi_4^{\mathrm{Na}}(t)}{\sqrt{N_{\mathrm{Na}}}},\\
\frac{dY_{11}}{dt} &= 3\alpha_m Y_{01} - \beta_m Y_{11} - 2\alpha_m Y_{11} + 2\beta_m Y_{21} + \alpha_h Y_{10} - \beta_h Y_{11} - \sqrt{3\alpha_m Y_{01} + \beta_m Y_{11}}\frac{\xi_8^{\mathrm{Na}}(t)}{\sqrt{N_{\mathrm{Na}}}}\\
&\quad + \sqrt{2\alpha_m Y_{11} + 2\beta_m Y_{21}}\frac{\xi_9^{\mathrm{Na}}(t)}{\sqrt{N_{\mathrm{Na}}}} - \sqrt{\alpha_h Y_{10} + \beta_h Y_{11}}\frac{\xi_5^{\mathrm{Na}}(t)}{\sqrt{N_{\mathrm{Na}}}},\\
\frac{dY_{21}}{dt} &= 2\alpha_m Y_{11} - 2\beta_m Y_{21} - \alpha_m Y_{21} + 3\beta_m Y_{31} + \alpha_h Y_{20} - \beta_h Y_{21} - \sqrt{2\alpha_m Y_{11} + 2\beta_m Y_{21}}\frac{\xi_9^{\mathrm{Na}}(t)}{\sqrt{N_{\mathrm{Na}}}}\\
&\quad + \sqrt{\alpha_m Y_{21} + 3\beta_m Y_{31}}\frac{\xi_{10}^{\mathrm{Na}}(t)}{\sqrt{N_{\mathrm{Na}}}} - \sqrt{\alpha_h Y_{20} + \beta_h Y_{21}}\frac{\xi_6^{\mathrm{Na}}(t)}{\sqrt{N_{\mathrm{Na}}}},\\
\frac{dY_{31}}{dt} &= \alpha_m Y_{21} - 3\beta_m Y_{31} + \alpha_h Y_{30} - \beta_h Y_{31} - \sqrt{\alpha_m Y_{21} + 3\beta_m Y_{31}}\frac{\xi_{10}^{\mathrm{Na}}(t)}{\sqrt{N_{\mathrm{Na}}}} - \sqrt{\alpha_h Y_{30} + \beta_h Y_{31}}\frac{\xi_7^{\mathrm{Na}}(t)}{\sqrt{N_{\mathrm{Na}}}},\\
\frac{d\tilde{R}}{dt} &= -\frac{1}{\tau}(\tilde{R} - \mu_R) + \sqrt{D}\,\xi_{\tilde{\mathrm{R}}}(t),
\end{aligned}
$$

where the voltage dependence of the α and β state transition rates (see Table I) has been suppressed for clarity. Note that the potassium channel equations contain 5 variables and 4 independent Gaussian white-noise terms ξ_i^{K} for $i \in \{1,2,3,4\}$ while the sodium equations contain 8 variables and 10 such terms ξ_i^{Na} for $i \in \{1,2,\ldots,10\}$. We seek to write this system as

$$
\begin{bmatrix} \dot{Z}_1(t) \\ \vdots \\ \dot{Z}_{15}(t) \end{bmatrix} = \begin{bmatrix} F_1 \\ \vdots \\ F_{15} \end{bmatrix} + \begin{bmatrix} 0 & 0 & 0 & 0 \\ 0 & \mathbf{S}_{\mathrm{K}} & 0 & 0 \\ 0 & 0 & \mathbf{S}_{\mathrm{Na}} & 0 \\ 0 & 0 & 0 & \sqrt{D} \end{bmatrix} \begin{bmatrix} 0 \\ \Xi_{\mathrm{K}}(t) \\ \Xi_{\mathrm{Na}}(t) \\ \xi_{\tilde{R}}(t) \end{bmatrix} \quad \leftrightarrow \quad \dot{\mathbf{Z}}(t) = \mathbf{F} + \mathbf{S}\,\Xi(t),
$$

where $\dot{\mathbf{Z}}(t) = d\mathbf{Z}/dt$ is a column vector containing the first time derivative of each state variable Z_i for $i \in \{1,2,\ldots,15\}$; $\mathbf{S} = \mathrm{diag}(0,\mathbf{S}_{\mathrm{K}},\mathbf{S}_{\mathrm{Na}},\sqrt{D})$ is a matrix that controls the magnitudes of the additive Gaussian white-noise terms; $\Xi = [0,\Xi_{\mathrm{K}},\Xi_{\mathrm{Na}},\xi_{\tilde{R}}]^{\mathrm{T}}$ is a column vector containing the Gaussian white-noise terms with $\Xi_{\mathrm{K}} = [\xi_1^{\mathrm{K}},\ldots,\xi_4^{\mathrm{K}}]^{\mathrm{T}}$ and $\Xi_{\mathrm{Na}} = [\xi_1^{\mathrm{Na}},\ldots,\xi_{10}^{\mathrm{Na}}]^{\mathrm{T}}$; and $\mathbf{F}$ is a column vector containing the deterministic portions of the original equations. The $\mathbf{S}$ matrix is 15×17 due to the nonsquare dimensions of $\mathbf{S}_{\mathrm{Na}}$ which itself is 8×10. The $\mathbf{S}_{\mathrm{K}}$ and $\mathbf{S}_{\mathrm{Na}}$ matrices are structured as follows:

$$
\mathbf{S}_{\mathrm{K}} = \frac{1}{\sqrt{N_{\mathrm{K}}}} \begin{bmatrix} 0 & x_1 & 0 & 0 & 0 \\ 0 & -x_1 & x_2 & 0 & 0 \\ 0 & 0 & -x_2 & x_3 & 0 \\ 0 & 0 & 0 & -x_3 & x_4 \\ 0 & 0 & 0 & 0 & -x_4 \end{bmatrix},
$$

$$
\mathbf{S}_{\mathrm{Na}} = \frac{1}{\sqrt{N_{\mathrm{Na}}}} \begin{bmatrix} y_1 & 0 & 0 & y_4 & 0 & 0 & 0 & 0 & 0 & 0 \\ -y_1 & y_2 & 0 & 0 & y_5 & 0 & 0 & 0 & 0 & 0 \\ 0 & -y_2 & y_3 & 0 & 0 & y_6 & 0 & 0 & 0 & 0 \\ 0 & 0 & -y_3 & 0 & 0 & 0 & y_7 & 0 & 0 & 0 \\ 0 & 0 & 0 & -y_4 & 0 & 0 & 0 & y_8 & 0 & 0 \\ 0 & 0 & 0 & 0 & -y_5 & 0 & 0 & -y_8 & y_9 & 0 \\ 0 & 0 & 0 & 0 & 0 & -y_6 & 0 & 0 & -y_9 & y_{10} \\ 0 & 0 & 0 & 0 & 0 & 0 & -y_7 & 0 & 0 & -y_{10} \end{bmatrix}.
$$

The matrix elements of $\mathbf{S}_{\mathrm{K}}$ are

$$
\begin{aligned}
x_1 &= \sqrt{4\alpha_n X_0 + \beta_n X_1},\\
x_2 &= \sqrt{3\alpha_n X_1 + 2\beta_n X_2},\\
x_3 &= \sqrt{2\alpha_n X_2 + 3\beta_n X_3},\\
x_4 &= \sqrt{\alpha_n X_3 + 4\beta_n X_4},
\end{aligned}
$$

and those of $\mathbf{S}_{\mathrm{Na}}$ are

$$
\begin{aligned}
y_1 &= \sqrt{3\alpha_m Y_{00} + \beta_m Y_{10}},\\
y_2 &= \sqrt{2\alpha_m Y_{10} + 2\beta_m Y_{20}},\\
y_3 &= \sqrt{\alpha_m Y_{20} + 3\beta_m Y_{30}},\\
y_4 &= \sqrt{\alpha_h Y_{00} + \beta_h Y_{01}},
\end{aligned}
$$

$$y_5 = \sqrt{\alpha_h Y_{10} + \beta_h Y_{11}},$$
$$y_6 = \sqrt{\alpha_h Y_{20} + \beta_h Y_{21}},$$
$$y_7 = \sqrt{\alpha_h Y_{30} + \beta_h Y_{31}},$$
$$y_8 = \sqrt{3\alpha_m Y_{01} + \beta_m Y_{11}},$$
$$y_9 = \sqrt{2\alpha_m Y_{11} + 2\beta_m Y_{21}},$$
$$y_{10} = \sqrt{\alpha_m Y_{21} + 3\beta_m Y_{31}}.$$

Finally, the elements of the vector $\mathbf{F}$ are

$$\begin{aligned}
F_1 &= \frac{1}{C}\{I_{\mathrm{DC}} - \bar{g}_{\mathrm{Na}} Y_{31}(V - E_{\mathrm{Na}}) \\
&\quad - \bar{g}_{\mathrm{K}} X_4 (V - E_{\mathrm{K}}) - g_{\mathrm{L}}(V - E_{\mathrm{L}}) \\
&\quad - \bar{g}_{\mathrm{GABA}} \tilde{R}\,(V - E_{\mathrm{GABA}})\}, \\
F_2 &= -4\alpha_n X_0 + \beta_n X_1, \\
F_3 &= 4\alpha_n X_0 - \beta_n X_1 - 3\alpha_n X_1 + 2\beta_n X_2, \\
F_4 &= 3\alpha_n X_1 - 2\beta_n X_2 - 2\alpha_n X_2 + 3\beta_n X_3, \\
F_5 &= 2\alpha_n X_2 - 3\beta_n X_3 - \alpha_n X_3 + 4\beta_n X_4, \\
F_6 &= \alpha_n X_3 - 4\beta_n X_4, \\
F_7 &= -3\alpha_m Y_{00} + \beta_m Y_{10} - \alpha_h Y_{00} + \beta_h Y_{01}, \\
F_8 &= 3\alpha_m Y_{00} - \beta_m Y_{10} - 2\alpha_m Y_{10} + 2\beta_m Y_{20} \\
&\quad - \alpha_h Y_{10} + \beta_h Y_{11}, \\
F_9 &= 2\alpha_m Y_{10} - 2\beta_m Y_{20} - \alpha_m Y_{20} + 3\beta_m Y_{30} \\
&\quad - \alpha_h Y_{20} + \beta_h Y_{21}, \\
F_{10} &= \alpha_m Y_{20} - 3\beta_m Y_{30} - \alpha_h Y_{30} + \beta_h Y_{31}, \\
F_{11} &= -3\alpha_m Y_{01} + \beta_m Y_{11} + \alpha_h Y_{00} - \beta_h Y_{01}, \\
F_{12} &= 3\alpha_m Y_{01} - \beta_m Y_{11} - 2\alpha_m Y_{11} + 2\beta_m Y_{21} \\
&\quad + \alpha_h Y_{10} - \beta_h Y_{11}, \\
F_{13} &= 2\alpha_m Y_{11} - 2\beta_m Y_{21} - \alpha_m Y_{21} + 3\beta_m Y_{31} \\
&\quad + \alpha_h Y_{20} - \beta_h Y_{21}, \\
F_{14} &= \alpha_m Y_{21} - 3\beta_m Y_{31} + \alpha_h Y_{30} - \beta_h Y_{31}, \\
F_{15} &= -\frac{1}{\tau}(\tilde{R} - \mu_R).
\end{aligned}$$

For each subthreshold input current-density $I_{\mathrm{DC}} < I_{\mathrm{DC}}^{\mathrm{crit}}$, the equilibrium state $\mathbf{Z}^0 = [V^0, X_0^0, \ldots, Y_{31}^0, \tilde{R}^0]^{\mathrm{T}}$ is given by the solution to the deterministic system $\mathbf{F} = 0$. Temporarily setting the additive noise terms to zero and expanding the remaining equations to first order in the variable $\mathbf{z}(t) = \mathbf{Z}(t) - \mathbf{Z}^0$, representing the instantaneous fluctuation of each state variable about its steady-state value, gives

$$\frac{d}{dt}\mathbf{z}(t) = \mathbf{J}\mathbf{z}(t) + \mathbf{S}\Xi(t)$$

as the linearized version of the approximating system where $\mathbf{J}$ is the Jacobian matrix of the deterministic system $\dot{\mathbf{Z}}(t) = \mathbf{F}$. Formulating this equation as a conventional Ornstein-Uhlenbeck process gives

$$\frac{d}{dt}\mathbf{z}(t) = -\mathbf{A}\mathbf{z}(t) + \sqrt{\mathbf{D}}\,\Xi(t),$$

where $\mathbf{A} = -\mathbf{J}$ is the drift matrix and $\mathbf{D} = \mathbf{S}^2$ is the diffusion matrix [compare to Eq. (12)]. Note that in practice, the normalization conditions on the $\mathbf{X}_{\mathrm{K}}$ and $\mathbf{Y}_{\mathrm{Na}}$ vectors are used to reduce the dimensionality of this system from 15 to 13 state variables.

In its fully expanded form—taking the sodium and potassium state vector normalization conditions into account to eliminate the X_0 and Y_{00} states—the 13×13 Jacobian matrix, $\mathbf{J}$, of the linearized system is

$$\mathbf{J} = \left.\frac{\partial(F_V, F_{X_1}, F_{X_2}, F_{X_3}, F_{X_4}, F_{Y_{10}}, F_{Y_{20}}, F_{Y_{30}}, F_{Y_{01}}, F_{Y_{11}}, F_{Y_{21}}, F_{Y_{31}}, F_{\tilde{R}})}{\partial(V, X_1, X_2, X_3, X_4, Y_{10}, Y_{20}, Y_{30}, Y_{01}, Y_{11}, Y_{21}, Y_{31}, \tilde{R})}\right|_{\mathbf{Z}^0},$$

where, importantly, evaluation occurs at the deterministic equilibrium state $\mathbf{Z}^0$ defined by I_{DC}. Of the $13^2 = 169$ Jacobian matrix elements, only 60 are nonzero giving $\mathbf{J}$ the following general form:

$$\mathbf{J} = \begin{bmatrix}
\mathrm{J}_{1,1} & 0 & 0 & 0 & \mathrm{J}_{1,5} & 0 & 0 & 0 & 0 & 0 & 0 & \mathrm{J}_{1,12} & \mathrm{J}_{1,13} \\
\mathrm{J}_{2,1} & \mathrm{J}_{2,2} & \mathrm{J}_{2,3} & \mathrm{J}_{2,4} & \mathrm{J}_{2,5} & 0 & 0 & 0 & 0 & 0 & 0 & 0 & 0 \\
\mathrm{J}_{3,1} & \mathrm{J}_{3,2} & \mathrm{J}_{3,3} & \mathrm{J}_{3,4} & 0 & 0 & 0 & 0 & 0 & 0 & 0 & 0 & 0 \\
\mathrm{J}_{4,1} & 0 & \mathrm{J}_{4,3} & \mathrm{J}_{4,4} & \mathrm{J}_{4,5} & 0 & 0 & 0 & 0 & 0 & 0 & 0 & 0 \\
\mathrm{J}_{5,1} & 0 & 0 & \mathrm{J}_{5,4} & \mathrm{J}_{5,5} & 0 & 0 & 0 & 0 & 0 & 0 & 0 & 0 \\
\mathrm{J}_{6,1} & 0 & 0 & 0 & 0 & \mathrm{J}_{6,6} & \mathrm{J}_{6,7} & \mathrm{J}_{7,8} & \mathrm{J}_{6,9} & \mathrm{J}_{6,10} & \mathrm{J}_{6,10} & \mathrm{J}_{6,12} & 0 \\
\mathrm{J}_{7,1} & 0 & 0 & 0 & 0 & \mathrm{J}_{7,6} & \mathrm{J}_{7,7} & \mathrm{J}_{7,8} & 0 & 0 & \mathrm{J}_{7,11} & 0 & 0 \\
\mathrm{J}_{8,1} & 0 & 0 & 0 & 0 & 0 & \mathrm{J}_{8,7} & \mathrm{J}_{8,8} & 0 & 0 & 0 & \mathrm{J}_{8,12} & 0 \\
\mathrm{J}_{9,1} & 0 & 0 & 0 & 0 & \mathrm{J}_{9,6} & \mathrm{J}_{9,7} & \mathrm{J}_{9,8} & \mathrm{J}_{9,9} & \mathrm{J}_{9,10} & \mathrm{J}_{9,11} & \mathrm{J}_{9,12} & 0 \\
\mathrm{J}_{10,1} & 0 & 0 & 0 & 0 & \mathrm{J}_{10,6} & 0 & 0 & \mathrm{J}_{10,9} & \mathrm{J}_{10,10} & \mathrm{J}_{10,11} & 0 & 0 \\
\mathrm{J}_{11,1} & 0 & 0 & 0 & 0 & 0 & \mathrm{J}_{11,7} & 0 & 0 & \mathrm{J}_{11,10} & \mathrm{J}_{11,11} & \mathrm{J}_{11,12} & 0 \\
\mathrm{J}_{12,1} & 0 & 0 & 0 & 0 & 0 & 0 & \mathrm{J}_{12,8} & 0 & 0 & \mathrm{J}_{12,11} & \mathrm{J}_{12,12} & 0 \\
0 & 0 & 0 & 0 & 0 & 0 & 0 & 0 & 0 & 0 & 0 & 0 & \mathrm{J}_{13,13}
\end{bmatrix},$$

with nonzero entries

$$\begin{aligned}
\mathrm{J}_{1,1} &= -(\bar{g}_{\mathrm{Na}} Y_{31} + \bar{g}_{\mathrm{K}} X_4 + g_{\mathrm{L}} + \bar{g}_{\mathrm{GABA}} \mu_R)/C, \\
\mathrm{J}_{1,5} &= \bar{g}_{\mathrm{K}}(E_{\mathrm{K}} - V)/C, \\
\mathrm{J}_{1,12} &= \bar{g}_{\mathrm{Na}}(E_{\mathrm{Na}} - V)/C, \\
\mathrm{J}_{1,13} &= \bar{g}_{\mathrm{GABA}}(E_{\mathrm{GABA}} - V)/C,
\end{aligned}$$

$$\begin{aligned}
\mathrm{J}_{2,1} &= 4\dot{\alpha}_n(1 - X_3 - X_4) + (2\dot{\beta}_n - 4\dot{\alpha}_n)X_2 - (7\dot{\alpha}_n + \dot{\beta}_n)X_1, \\
\mathrm{J}_{2,2} &= -(7\alpha_n + \beta_n), \\
\mathrm{J}_{2,3} &= 2\beta_n - 4\alpha_n, \\
\mathrm{J}_{2,4} &= -4\alpha_n, \\
\mathrm{J}_{2,5} &= -4\alpha_n,
\end{aligned}$$

$$\begin{aligned}
\mathrm{J}_{3,1} &= 3\dot{\alpha}_n X_1 + 3\dot{\beta}_n X_3 - 2(\dot{\alpha}_n + \dot{\beta}_n)X_2, \\
\mathrm{J}_{3,2} &= 3\alpha_n, \\
\mathrm{J}_{3,3} &= -2(\alpha_n + \beta_n), \\
\mathrm{J}_{3,4} &= 3\beta_n,
\end{aligned}$$

$$\begin{aligned}
\mathrm{J}_{4,1} &= 2\dot{\alpha}_n X_2 + 4\dot{\beta}_n X_4 - (\dot{\alpha}_n + 3\dot{\beta}_n)X_3, \\
\mathrm{J}_{4,3} &= 2\alpha_n, \\
\mathrm{J}_{4,4} &= -(\alpha_n + 3\beta_n), \\
\mathrm{J}_{4,5} &= 4\beta_n,
\end{aligned}$$

$$\begin{aligned}
\mathrm{J}_{5,1} &= \dot{\alpha}_n X_3 - 4\dot{\beta}_n X_4, \\
\mathrm{J}_{5,4} &= \alpha_n, \\
\mathrm{J}_{5,5} &= -4\beta_n,
\end{aligned}$$

$$\begin{aligned}
\mathrm{J}_{6,1} &= 3\dot{\alpha}_m(1 - Y_{30} - Y_{01} - Y_{21} - Y_{31}) \\
&\quad + (2\dot{\beta}_m - 3\dot{\alpha}_m)Y_{20} + (\dot{\beta}_h - 3\dot{\alpha}_m)Y_{11} \\
&\quad - (5\dot{\alpha}_m + \dot{\beta}_m + \dot{\alpha}_h)Y_{10}, \\
\mathrm{J}_{6,6} &= -(5\alpha_m + \beta_m + \alpha_h), \\
\mathrm{J}_{6,7} &= 2\beta_m - 3\alpha_m, \\
\mathrm{J}_{6,8} &= -3\alpha_m, \\
\mathrm{J}_{6,9} &= -3\alpha_m, \\
\mathrm{J}_{6,10} &= \beta_h - 3\alpha_m, \\
\mathrm{J}_{6,11} &= -3\alpha_m, \\
\mathrm{J}_{6,12} &= -3\alpha_m,
\end{aligned}$$

$$\begin{aligned}
\mathrm{J}_{7,1} &= 2\dot{\alpha}_m Y_{10} + 3\dot{\beta}_m Y_{30} + \dot{\beta}_h Y_{21} \\
&\quad - (\dot{\alpha}_m + 2\dot{\beta}_m + \dot{\alpha}_h)Y_{20}, \\
\mathrm{J}_{7,6} &= 2\alpha_m, \\
\mathrm{J}_{7,7} &= -(\alpha_m + 2\beta_m + \alpha_h), \\
\mathrm{J}_{7,8} &= 3\beta_m, \\
\mathrm{J}_{7,11} &= \beta_h,
\end{aligned}$$

$$\begin{aligned}
\mathrm{J}_{8,1} &= \dot{\alpha}_m Y_{20} + \dot{\beta}_h Y_{31} - (3\dot{\beta}_m + \dot{\alpha}_h)Y_{30}, \\
\mathrm{J}_{8,7} &= \alpha_m, \\
\mathrm{J}_{8,8} &= -(3\beta_m + \alpha_h), \\
\mathrm{J}_{8,12} &= \beta_h,
\end{aligned}$$

$$\begin{aligned}
\mathrm{J}_{9,1} &= \dot{\alpha}_h(1 - Y_{10} - Y_{20} - Y_{30} - Y_{21} - Y_{31}) \\
&\quad + (\dot{\beta}_m - \dot{\alpha}_h)Y_{11} - (3\dot{\alpha}_m + \dot{\beta}_h + \dot{\alpha}_h)Y_{01}, \\
\mathrm{J}_{9,6} &= -\alpha_h, \\
\mathrm{J}_{9,7} &= -\alpha_h, \\
\mathrm{J}_{9,8} &= -\alpha_h, \\
\mathrm{J}_{9,9} &= -(3\alpha_m + \beta_h + \alpha_h), \\
\mathrm{J}_{9,10} &= \beta_m - \alpha_h, \\
\mathrm{J}_{9,11} &= -\alpha_h, \\
\mathrm{J}_{9,12} &= -\alpha_h,
\end{aligned}$$

$$\begin{aligned}
\mathrm{J}_{10,1} &= \dot{\alpha}_h Y_{10} + 3\dot{\alpha}_m Y_{01} + 2\dot{\beta}_m Y_{21} \\
&\quad - (2\dot{\alpha}_m + \dot{\beta}_m + \dot{\beta}_h)Y_{11}, \\
\mathrm{J}_{10,6} &= \alpha_h, \\
\mathrm{J}_{10,9} &= 3\alpha_m, \\
\mathrm{J}_{10,10} &= -(2\alpha_m + \beta_m + \beta_h), \\
\mathrm{J}_{10,11} &= 2\beta_m,
\end{aligned}$$

$$\begin{aligned}
\mathrm{J}_{11,1} &= \dot{\alpha}_h Y_{20} + 2\dot{\alpha}_m Y_{11} + 3\dot{\beta}_m Y_{31} \\
&\quad - (\dot{\alpha}_m + 2\dot{\beta}_m + \dot{\beta}_h)Y_{21}, \\
\mathrm{J}_{11,7} &= \alpha_h, \\
\mathrm{J}_{11,10} &= 2\alpha_m, \\
\mathrm{J}_{11,11} &= -(\alpha_m + 2\beta_m + \beta_h), \\
\mathrm{J}_{11,12} &= 3\beta_m,
\end{aligned}$$

$$\begin{aligned}
\mathrm{J}_{12,1} &= \dot{\alpha}_h Y_{30} + \dot{\alpha}_m Y_{21} - (3\dot{\beta}_m + \dot{\beta}_h)Y_{31}, \\
\mathrm{J}_{12,8} &= \alpha_h, \\
\mathrm{J}_{12,11} &= \alpha_m, \\
\mathrm{J}_{12,12} &= -(3\beta_m + \beta_h),
\end{aligned}$$

$$\mathrm{J}_{13,13} = -1/\tau.$$

Here dot notation has been used to indicate first derivatives with respect to voltage [e.g., $\dot{\alpha}_n = d\alpha_n(V)/dV$].

[1] H. C. Hemmings, Molecular targets of general anesthetics in the nervous system, in *Suppressing the Mind: Anesthetic Modulation of Memory and Consciousness*, edited by Anthony Hudetz and Robert Pearce (Humana Press, New York, 2010), Chap. 2, pp. 11–31.

[2] N. P. Franks and W. R. Lieb, Molecular and cellular mechanisms of general anesthesia, Nature (London) **367**, 607 (1994).

[3] M. Farrant and Z. Nusser, Variations on an inhibitory theme: Phasic and tonic activation of $\mathrm{GABA_A}$ receptors, Nat. Rev. Neurosci. **6**, 215 (2005).

[4] A. Kitamura, W. Marszalec, J. Z. Yeh, and T. Narahashi, Effects of halothane and propofol on excitatory and inhibitory synaptic transmission in rat cortical neurons, Journal of Pharmacology and Experimental Therapeutics **304**, 161 (2003).

[5] M. L. Steyn-Ross, D. A. Steyn-Ross, J. W. Sleigh, and D. T. J. Liley, Theoretical electroencephalogram stationary spectrum for a white-noise-driven cortex: Evidence for a general anesthetic-induced phase transition, Phys. Rev. E **60**, 7299 (1999).

[6] I. Bojak and D. T. J. Liley, Modeling the effects of anesthesia on the electroencephalogram, Phys. Rev. E **71**, 041902 (2005).

[7] B. L. Foster, I. Bojak, and D. T. J. Liley, Population based models of cortical drug response: Insights from anaesthesia, Cognitive Neurodynamics **2**, 283 (2008).

[8] R. Hindriks and M. J. A. M. van Putten, Meanfield modeling of propofol-induced changes in spontaneous EEG rhythms, NeuroImage **60**, 2323 (2012).

[9] A. Hutt and A. Longtin, Effects of the anesthetic agent propofol on neural populations, Cognitive Neurodynamics **4**, 37 (2010).

[10] B. Molaee-Ardekani, L. Senhadji, M. B. Shamsollahi, B. Vosoughi-Vahdat, and E. Wodey, Brain activity modeling in general anesthesia: Enhancing local mean-field models using a slow adaptive firing rate, Phys. Rev. E **76**, 041911 (2007).

[11] M. M. McCarthy and N. Kopell, The effect of propofol anesthesia on rebound spiking, SIAM Journal of Applied Dynamical Systems **11**, 1674 (2012).

[12] A. Gottschalk and P. Haney, Computational aspects of anesthetic action in simple neural models, Anesthesiology **98**, 548 (2003).

[13] A. Hutt and L. Buhry, Study of GABAergic extra-synaptic tonic inhibition in single neurons and neural populations by traversing neural scales: Application to propofol-induced anaesthesia, J. Comput. Neurosci. **37**, 417 (2014).

[14] G. Matsumoto and T. Kunisawa, Critical slowing-down near the transition region from the resting to time-ordered states in squid giant axons, J. Phys. Soc. Jpn. **44**, 1047 (1978).

[15] C. Meisel, A. Klaus, C. Kuehn, and D. Plenz, Critical slowing down governs the transition to neuron spiking, PLoS Computational Biology **11**, e1004097 (2015).

[16] D. A. Steyn-Ross, M. L. Steyn-Ross, M. T. Wilson, and J. W. Sleigh, White-noise susceptibility and critical slowing in neurons near spiking threshold, Phys. Rev. E **74**, 051920 (2006).

[17] A. Bukoski, D. A. Steyn-Ross, and M. L. Steyn-Ross, Channel-noise-induced critical slowing in the subthreshold Hodgkin-Huxley neuron, Phys. Rev. E **91**, 032708 (2015).

[18] K. Kuizenga, C. J. Kalkman, and P. J. Hennis, Quantitative electroencephalographic analysis of the biphasic concentration-effect relationship of propofol in surgical patients during extradural analgesia, British Journal of Anaesthesia **80**, 725 (1998).

[19] K. Kuizenga, J. M. K. H. Wierda, and C. J. Kalkman, Biphasic EEG changes in relation to loss of consciousness during induction with thiopental, propofol, etomidate, midazolam, or sevoflurane, British Journal of Anaesthesia **86**, 354 (2001).

[20] M. L. Steyn-Ross, D. A. Steyn-Ross, J. W. Sleigh, and L. C. Wilcocks, Toward a theory of the general-anesthetic-induced phase transition of the cerebral cortex. I. A thermodynamics analogy, Phys. Rev. E **64**, 011917 (2001).

[21] D. A. Steyn-Ross, M. L. Steyn-Ross, L. C. Wilcocks, and J. W. Sleigh, Toward a theory of the general-anesthetic-induced phase transition of the cerebral cortex. II. Numerical simulations, spectral entropy, and correlation times, Phys. Rev. E **64**, 011918 (2001).

[22] A. L. Hodgkin and A. F. Huxley, A quantitative description of membrane current and its application to conduction and excitation in nerve, J. Physiol. **117**, 500 (1952).

[23] D. T. Gillespie, Exact stochastic simulation of coupled chemical reactions, J. Phys. Chem. **81**, 2340 (1977).

[24] R. F. Fox and Y.-N. Lu, Emergent collective behavior in large numbers of globally coupled independently stochastic ion channels, Phys. Rev. E **49**, 3421 (1994).

[25] P. Orio and D. Soudry, Simple, fast and accurate implementation of the diffusion approximation algorithm for stochastic ion channels with multiple states, PLoS ONE **7**, e36670 (2012).

[26] D. Pezo, D. Soudry, and P. Orio, Diffusion approximation-based simulation of stochastic ion channels: Which method to use? Frontiers in Computational Neuroscience **8**, 139 (2014).

[27] Y. Huang, S. Rüdiger, and J. Shuai, Accurate Langevin approaches to simulate Markovian channel dynamics, Physical Biology **12**, 061001 (2015).

[28] A. Destexhe, Z. F. Mainen, and T. J. Sejnowski, Kinetic models of synaptic transmission, in *Methods in Neuronal Modeling*, edited by C. Koch and I. Segev (MIT Press, Cambridge, 1998), Chap. 1, pp. 1–25.

[29] T. Nowotny and M. I. Rabinovich, Dynamical Origin of Independent Spiking and Bursting Activity in Neural Microcircuits, Phys. Rev. Lett. **98**, 128106 (2007).

[30] T. Nowotny and M. I. Rabinovich, Erratum: Dynamical Origin of Independent Spiking and Bursting Activity in Neural Microcircuits, Phys. Rev. Lett. **101**, 079901(E) (2008).

[31] C. Koch, *Biophysics of Computation: Information Processing in Single Neurons* (Oxford University Press, New York, 1999).

[32] A. Destexhe, M. Rudolph, J. M. Fellous, and T. J. Sejnowski, Fluctuating synaptic conductances recreate *in vivo*-like activity in neocortical neurons, Neuroscience **107**, 13 (2001).

[33] A. Destexhe and M. Rudolph-Lilith, *Neuronal Noise*, Springer Series in Computational Neuroscience, Vol. 8 (Springer, New York, 2012).

[34] C. Gardiner, *Stochastic Methods: A Handbook for the Natural and Social Sciences*, 4th ed. (Springer, Berlin, 2009).

[35] T. Tateno and K. Pakdaman, Random dynamics of the Morris-Lecar neural model, Chaos **14**, 511 (2004).

[36] H. C. Tuckwell, J. Jost, and B. S. Gutkin, Inhibition and modulation of rhythmic neuronal spiking by noise, Phys. Rev. E **80**, 031907 (2009).

[37] H. C. Tuckwell and S. Ditlevsen, The space-clamped Hodgkin-Huxley system with random synaptic input: Inhibition of spiking by weak noise and analysis with moment equations, Neural Comput. **28**, 2129 (2016).

[38] M. L. Steyn-Ross, D. A. Steyn-Ross, M. T. Wilson, and J. W. Sleigh, Gap junctions mediate large-scale Turing structures in a mean-field cortex driven by subcortical noise, Phys. Rev. E **76**, 011916 (2007).

[39] I. Aradi, V. Santhakumar, K. Chen, and I. Soltesz, Postsynaptic effects of GABAergic synaptic diversity: Regulation of neuronal excitability by changes in IPSC variance, Neuropharmacology **43**, 511 (2002).

[40] B. Rehberg and D. S. Duch, Suppression of central nervous system sodium channels by propofol, Anesthesiology **91**, 512 (1999).

[41] J. Andrada, P. Livingston, B. J. Lee, and J. Antognini, Propofol and etomidate depress cortical, thalamic, and reticular formation

neurons during anesthetic-induced unconsciousness, Anesthesia and Analgesia **114**, 661 (2012).

[42] K. P. Storer and G. N. Reeke, γ-Aminobutyric acid receptor type A receptor potentiation reduces firing of neuronal assemblies in a computational cortical model, Anesthesiology **117**, 780 (2012).

[43] R. Brette, Sharpness of spike initiation in neurons explained by compartmentalization, PLoS Comput. Biol. **9**, e1003338 (2013).

[44] R. Brette, What is the most realistic single-compartment model of spike initiation? PLoS Comput. Biol. **11**, e1004114 (2015).

[45] E. M. Izhikevich, *Dynamical Systems in Neuroscience* (MIT Press, Cambridge, 2007).

[46] V. Ilin, A. Malyshev, F. Wolf, and M. Volgushev, Fast computations in cortical ensembles require rapid initiation of action potentials, J. Neurosci. **33**, 2281 (2013).